

Kinetic equations in a third-generation spectral wave model

Qingxiang Liu^{1,†}, Odin Gramstad² and Alexander Babanin^{1,3}

¹Department of Infrastructure Engineering, University of Melbourne, VIC 3010, Australia

²Group Technology and Research, DNV GL, 1363 Høvik, Norway

³Laboratory for Regional Oceanography and Numerical Modeling, National Laboratory for Marine Science and Technology, 266237 Qingdao, PR China

(Received 30 June 2020; revised 5 October 2020; accepted 15 November 2020)

The Hasselmann kinetic equation (HKE) forms the cornerstone of present-day spectral wave models. It describes the redistribution of energy over the wave spectrum as a result of resonant four-wave interactions, and theoretically prescribes wave evolution on a slow $O(1/\varepsilon^4\omega_0)$ time scale, where ε and ω_0 are typical wave steepness and frequency. Alternatives to the HKE (e.g. the generalized kinetic equation (GKE)), including the effects of non-resonant four-wave interactions, are believed capable of evolving wave fields on a fast $O(1/\varepsilon^2\omega_0)$ time scale. It is beyond doubt that these alternatives could reasonably predict changes of unidirectional waves whereas the HKE cannot. For angular spread wave fields, however, it is still ambiguous whether the GKE behaves remarkably differently from the HKE because previous research in this direction was not fully consistent. In this study, we revised the GKE algorithm implemented in the spectral wave model WAVEWATCH III (WW3) by correcting two numerical aspects related to the discretization of the GKE and to the source term integration. It is proved that once updated, the GKE in WW3 does not give rise to significant deviation from the HKE-based results, provided that the wave spectra are fairly smooth and the directionality is sufficiently broad. These results, although unexpected, are in good agreement with findings reported by Annenkov & Shrira. More strikingly, the HKE and GKE are observed to operate at the same fast $O(1/\varepsilon^2\omega_0)$ time scale for the spectral peak downshift and angular broadening, indicating that the HKE, solved by the well-established Webb–Resio–Tracy algorithm, seems more robust than usually expected.

Key words: surface gravity waves

† Email addresses for correspondence: qingxiang.liu@unimelb.edu.au, qxiangliu@gmail.com

1. Introduction

The present-day third-generation spectral wave models generally solve the action balance equation (e.g. Komen *et al.* 1994; Janssen 2008) to predict the evolution of ocean surface waves:

$$\frac{dN}{dt} = \frac{S_{in} + S_{ds} + S_{nl} + \dots}{\omega}, \tag{1.1}$$

where $N(k, \theta; \mathbf{x}, t) = F(k, \theta; \mathbf{x}, t)/\omega$ is the wave action density spectrum, ω is the intrinsic (radian) frequency, $k = |\mathbf{k}|$ is the wavenumber and θ is the propagation direction of wave energy. For deep-water waves, ω and k are linked through the linear dispersion relation

$$\omega^2 = gk, \tag{1.2}$$

where g is the gravitational acceleration. The right-hand side of (1.1) consists of sources and sinks of wave energy, including wind input S_{in} , wave breaking-induced dissipation S_{ds} and nonlinear four-wave interaction S_{nl} (e.g. Cavaleri *et al.* 2007, 2018). Among these various physical processes, S_{nl} is known to play a central role in the development of wind-generated wave spectrum through controlling the downshifting of the spectral peak, the angular spreading and the high-frequency spectral tail (Hasselmann *et al.* 1973; Young & van Vledder 1993; Badulin *et al.* 2005, 2007).

The mathematical formulation of the nonlinear transfer S_{nl} for a continuous wave spectrum that describes how wave energy is redistributed over the spectral space due to resonant four-wave interactions was first established by Hasselmann (1962):

$$\frac{dC_1}{dt} = 4\pi \int \left[T_{1,2,3,4}^2 \mathcal{F}_{1,2,3,4} \delta(\Delta \mathbf{k}) \delta(\Delta \omega) \right] d\mathbf{k}_{2,3,4}, \tag{1.3}$$

$$\mathcal{F}_{1,2,3,4} = C_3 C_4 (C_1 + C_2) - C_1 C_2 (C_3 + C_4), \tag{1.4}$$

where $C_1 = C(\mathbf{k}_1) = gN(k, \theta)/k$ is the action spectrum, $T_{1,2,3,4} = T(\mathbf{k}_1, \mathbf{k}_2, \mathbf{k}_3, \mathbf{k}_4)$ is the interaction coefficient (Krasitskii 1994; Janssen 2009), $\Delta \mathbf{k} = \mathbf{k}_1 + \mathbf{k}_2 - \mathbf{k}_3 - \mathbf{k}_4$ and $\Delta \omega = \omega_1 + \omega_2 - \omega_3 - \omega_4$ are wavenumber and frequency mismatch and $d\mathbf{k}_{2,3,4} = dk_2 dk_3 dk_4$. The two δ -functions in (1.3) dictate that only four resonant wave components satisfying

$$\left. \begin{aligned} \mathbf{k}_1 + \mathbf{k}_2 &= \mathbf{k}_3 + \mathbf{k}_4, \\ \omega_1 + \omega_2 &= \omega_3 + \omega_4, \end{aligned} \right\} \tag{1.5}$$

could exchange energy and momentum. The Hasselmann equation (1.3) is also known as the standard kinetic equation and Boltzmann integral for a homogeneous, quasi-Gaussian wave field. Hereafter, we refer to it as the Hasselmann kinetic equation (HKE). According to (1.1) and (1.3), we have

$$S_{nl}(k, \theta) = \omega \left. \frac{dN}{dt} \right|_{nl} = \frac{\omega k}{g} \frac{dC_1}{dt}. \tag{1.6}$$

An important hypothesis underpinning the derivation of the HKE is the action density $C(\mathbf{k})$ evolves on a slow (‘kinetic’) time scale of $O(1/\varepsilon^4 \omega_0)$, where ε and ω_0 are typical wave steepness and frequency of the wave field (Annenkov & Shrira 2006). Consequently, as a large-time limit, the HKE does not include contributions from *non-resonant* interactions ($\Delta \omega \neq 0$).

Realizing the possible importance of non-resonant four-wave interactions for spectral evolution on a fast time scale $O(1/\varepsilon^2\omega_0)$, Janssen (2003) proposed to modify the HKE as

$$\frac{dC_1}{dt} = 4 \int \left[T_{1,2,3,4}^2 \mathcal{F}_{1,2,3,4} \delta(\Delta \mathbf{k}) R(\Delta \omega, t) \right] d\mathbf{k}_{2,3,4}, \quad (1.7)$$

where

$$R(\Delta \omega, t) = \text{Re} \int_0^t \exp(i\Delta \omega(t - \tau)) d\tau = \frac{\sin(\Delta \omega t)}{\Delta \omega}, \quad (1.8)$$

and

$$\left. \begin{aligned} \lim_{t \rightarrow 0} R(\Delta \omega, t) &= t, \\ \lim_{t \rightarrow \infty} R(\Delta \omega, t) &= \pi \delta(\Delta \omega). \end{aligned} \right\} \quad (1.9)$$

From (1.9) we know that (i) for short times Janssen’s kinetic equation (JKE) incorporates contributions from both resonant and non-resonant interactions, and (ii) the JKE is equivalent to the HKE for large times. In the context of a one-dimensional (1-D; unidirectional) wave spectrum, for which the HKE predicts no spectral change because of the non-existence of resonant quadruplets, Janssen (2003) demonstrated that his JKE could capture remarkably well the spectral evolution as revealed by direct simulations based on the Zakharov equation (Zakharov 1968).

It is noteworthy that the JKE still assumes the underlying action density $C(\mathbf{k})$ itself and, therefore, the action density product terms $\mathcal{F}_{1,2,3,4}$ (1.4) are slowly varying (i.e. quasi-stationary). Annenkov & Shrira (2006) further extended this kinetic equation by fully discarding the quasi-stationarity assumption, resulting in the so-called generalized kinetic equation (GKE). Later, Gramstad & Stiassnie (2013, hereafter GS13) advanced the GKE one-step further by taking into account high-order effects related to the Stokes correction of the frequencies. The authors, however, found the nonlinear Stokes correction not important for the cases they explored. Neglecting the effect of the Stokes-corrected frequencies, the GKE is formulated as (e.g. GS13):

$$\frac{dC_1}{dt} = 4\text{Re} \int \left[T_{1,2,3,4}^2 \delta(\Delta \mathbf{k}) \exp(i\Delta \omega t) I(t) \right] d\mathbf{k}_{2,3,4}, \quad (1.10)$$

$$I(t) = \int_0^t \mathcal{F}_{1,2,3,4}(\tau) \exp(-i\Delta \omega \tau) d\tau. \quad (1.11)$$

Here we have implicitly assumed a Gaussian initial condition such that the fourth-order cumulant and, hence, the time integral $I(t)$ are initially zero (see GS13 for more details). As summarized in table 1, the GKE not only includes the non-resonant interactions but also suggests the evolution of a wave field depends on its previous history of evolution (i.e. non-local in time; Annenkov & Shrira 2018, hereafter AS18). It is worth mentioning that the GKE will turn into the JKE if we take the action product term $\mathcal{F}_{1,2,3,4}$ in (1.11) outside the time integral and then will naturally become the HKE if we further adopt the large time limit (1.9).

The difference in the interaction space for the HKE and JKE/GKE is visualized in figure 1. As constrained by (1.5), for \mathbf{k}_1 and \mathbf{k}_3 fixed, the resonant \mathbf{k}_2 and \mathbf{k}_4 components will trace out two closed, ‘egg-shaped’ curves in wavenumber space (black lines in figure 1), which are referred to as loci in the literature (Webb 1978; van Vledder 2006). For the non-resonant quadruplets, which the JKE and GKE take into consideration but the HKE does not, there will be more numerous possible wavenumber configurations owing

Features	HKE	JKE	GKE
Resonant interactions	•	•	•
Non-resonant interactions	—	•	•
Non-locality of $C(k)$ in time	—	—	•

Table 1. Features included in different kinetic equations (nonlinear four-wave interaction transfer) for a homogenous, quasi-Gaussian wave field.

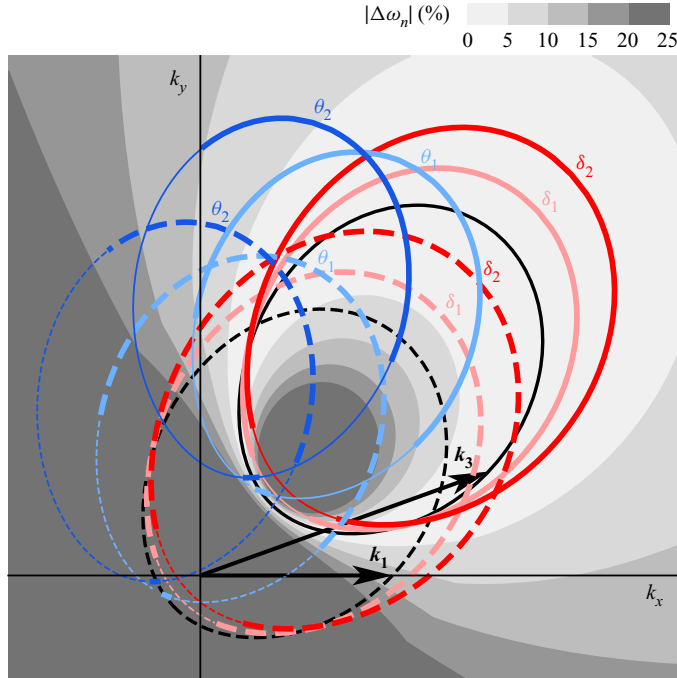


Figure 1. Illustration of the difference in the interaction space for the HKE and JKE/GKE for a given combination of k_1 (0.1, 0) and k_3 (0.15, 0.05) (adapted from figure 6 of van Vledder 2006). The black solid (dashed) line presents the locus for the resonant k_2 (k_4) component, computed with the polar method of van Vledder (2000). Shaded contour: the normalized frequency mismatch $|\Delta\omega_n| = |\Delta\omega|/\min(\omega_1, \omega_2, \omega_3, \omega_4)$. Red lines δ_i : the resonant k_2 locus is magnified by δ^i and $\delta = 1.1$, blue lines θ_j : the resonant k_2 locus is rotated counterclockwise through $\theta_j = 15^\circ j$ about the origin. The thick part of each coloured circle highlights the non-resonant quadruplets with $|\Delta\omega_n| \leq 0.1$.

to the removal of the δ -function over $\Delta\omega$. In essence, the non-resonant k_2 component can be any non-zero point in the wavenumber plane which does not fall on the resonant locus. For illustration purposes only, we also show a few subsets of non-resonant quadruplets in figure 1. For example, if we have $k_{2,nr} = \delta^i k_{2,r}$, $i = 1, 2, \dots$ and $\delta > 1$, where the subscripts ‘nr’ and ‘r’ denote non-resonant and resonant wave components, respectively, we obtain a family of newly formed, magnified loci for $k_{2,nr}$ and accordingly $k_{4,nr}$ (red lines in figure 1). Similarly, if we rotate the resonant k_2 locus counterclockwise through an angle $\theta_j = j\Delta\theta$, $j = 1, 2, \dots$ about the origin, another set of loci for $k_{2,nr}$ and $k_{4,nr}$ will be acquired (blue lines in figure 1). In practice, however, only non-resonant quadruplets that are not far from resonance (i.e. *quasi-resonant*) are considered (see § 2 for further explanation).

The first computation of two-dimensional (2-D) wave spectra with the GKE was performed by GS13. Gramstad & Babanin (2016, hereafter GB16) further implemented their GKE algorithm in the spectral wave model WAVEWATCH III (hereafter WW3, version 3.14; Tolman 2009), and reported remarkable differences between the HKE and GKE simulations for both directionally narrow and broad spectra, and for spectra subject to sudden changes in wind speed or direction. These results, however, are inconsistent with a series of work by Annenkov & Shrira (2015, 2016, 2018, 2019) who demonstrated that the GKE results are not significantly different from the HKE (in terms of spectral shape) even for steep, narrow-banded and directionally narrow wave fields. Therefore, it is still puzzling whether the quasi-resonant four-wave interactions and non-locality of $C(\mathbf{k})$, as incorporated by the GKE, are critical for development of 2-D wave spectra.

Motivated by these disputes, we revisited the GKE algorithm developed by GB16, rewrote it as a set of subroutines and then implemented them in WW3 (v6.07; WW3DG 2019). These efforts revealed that two numerical aspects pertaining to the discretization of the GKE and to the source term integration were not handled properly in GB16. Corrections of these non-trivial numerical aspects are proposed in this study; meanwhile, considering the high similarity between the JKE and GKE, we implement the JKE under the framework of the GKE in WW3 as well (§ 2). Comparisons of three kinetic equations (HKE, JKE, GKE) are then carefully investigated through (i) a duration-limited wave growth test (§ 3), (ii) adiabatic evolution of a steep Gaussian wave spectrum (§ 4), (iii) response of ocean waves to turning winds (§ 5) and (iv) development of ice-coupled waves (§ 6). Note that following Young (1999), the *duration-limited wave growth* here specifically refers to the case where the wave field is sufficiently distant from land boundaries and grows under a spatially homogeneous and stationary wind field (i.e. constant wind speed and direction). Other cases considered in the paper are still duration-limited (spatially homogeneous and no dependence on the spatial coordinate) but are subject to different external environmental forcing.

It is seen that good agreement with the findings of Annenkov & Shrira can be achieved with the updated GKE algorithm. As our GKE algorithm and that used by Annenkov & Shrira were developed fully independently, it appears reasonable to unambiguously conclude that beyond our expectation, corrections embraced in the present JKE/GKE relative to the HKE do not give rise to significantly different spectral evolution of directional wind waves, provided that wave spectra are fairly smooth (i.e. no strong perturbations) and the directionality is sufficiently broad. More detailed discussion and conclusions of these findings are given in §§ 7 and 8, respectively.

2. Numerical algorithm

2.1. The GKE

The GKE algorithm and its implementation in WW3, originally developed by GB16, together with relevant updates, are documented in the following subsections, including the discretization of equations, quasi-resonant filter, phase mixing and source term integration.

2.1.1. Discretization

According to (1.10), the incremental change of action δC_1 in an infinitesimal phase element $\delta \mathbf{k}_1$ and time interval Δt is

$$\delta C_1 = \frac{dC_1}{dt} \delta \mathbf{k}_1 \Delta t = 4\text{Re} \int \left[T_{1,2,3,4}^2 \delta(\Delta \mathbf{k}) \exp(i\Delta \omega t) I(t) \right] d\mathbf{k}_{2,3,4} \delta \mathbf{k}_1 \Delta t, \quad (2.1)$$

and owing to the symmetry of four-wave interactions (Hasselmann & Hasselmann 1985),

$$\delta C_1 = \delta C_2 = -\delta C_3 = -\delta C_4. \tag{2.2}$$

In this respect, GS13 and Janssen & Janssen (2019) reported that both the GKE and JKE conserve the total wave action, momentum and energy (see also Shrira & Annenkov 2013). Therefore, the principle of detailed balance (2.2) holds for these two equations, just as for the HKE. When implemented in WW3, (1.10) and (2.1) are discretized as

$$\frac{dC_1}{dt} = \sum_{k_{2,3,4}} \mathcal{M}_{1,2,3,4} / \delta k_1, \tag{2.3}$$

where δk is the area of the given wavenumber bin and

$$\mathcal{M}_{1,2,3,4} = 4T_{1,2,3,4}^2 \delta(\Delta k) \text{Re} [\exp(i\Delta\omega t) I(t)] \delta k_{1,2,3,4}. \tag{2.4}$$

The time integral $I(t)$ is solved iteratively by

$$\begin{aligned} I(t) &= I(t - \Delta t) + \int_{t-\Delta t}^t \mathcal{F}_{1,2,3,4}(\tau) \exp(-i\Delta\omega\tau) d\tau, \\ &= I(t - \Delta t) + \frac{\Delta t}{2} [\mathcal{F}_{1,2,3,4}(t - \Delta t) \exp(-i\Delta\omega(t - \Delta t)) + \mathcal{F}_{1,2,3,4}(t) \exp(-i\Delta\omega t)]. \end{aligned} \tag{2.5}$$

For an intermediate step of estimating (2.3)–(2.5), GB16 considered waves of different modes as discrete wave systems and have adopted

$$\sum_{k_{2,3,4}} \mathcal{F}_{1,2,3,4} \delta(\Delta k) \delta k_{1,2,3,4} = \sum_{k_{2,3,4}} C_3' C_4' (C_1' + C_2') - C_1' C_2' (C_3' + C_4'), \tag{2.6}$$

where $C'(k) = C(k)\delta k$. For discrete spectral wave models with a logarithmically spaced frequency grid, however, (2.6) should be more naturally solved by

$$\sum_{k_{2,3,4}} \mathcal{F}_{1,2,3,4} \delta(\Delta k) \delta k_{1,2,3,4} = \sum_{k_{2,3,4}} \mathcal{F}_{1,2,3,4} \delta k_{1,2,3}, \tag{2.7}$$

where the δ -function over wavenumber is eliminated because of

$$\int \delta(\Delta k) dk_4 = \int \delta(k_1 + k_2 - k_3 - k_4) dk_4 = 1 \tag{2.8}$$

according to Tracy & Resio (1982). Clearly, for an equally spaced wavenumber grid, (2.6) and (2.7) are equivalent. More technical details for solving (2.3)–(2.7) are presented in appendix A.

2.1.2. Filtration of quadruplets

To reduce the computational expense of the GKE, we only consider wavenumber configurations satisfying

$$\left. \begin{aligned} k_1 + k_2 &= k_3 + k_4, \\ |\Delta\omega| &\leq \lambda_c \min(\omega_1, \omega_2, \omega_3, \omega_4), \end{aligned} \right\} \tag{2.9}$$

as valid quadruplets. Here λ_c is a cut-off factor used to filter out quartets very far from resonance which contribute little to spectral evolution (figure 1). From a theoretical

point of view, GB16 suggested $\lambda_c = O(\varepsilon^2)$ (note that in generic situations $\Delta\omega \sim O(\varepsilon^2)$ (Annenkov & Shrira 2006)) and adopted $\lambda_c = 0.08$ for their simulations. Similarly, AS18 pointed out that for short-term simulations ($O(10^2)$ wave periods), λ_c of $O(10^{-2})$ is sufficient; instead, for better numerical stability a larger $O(10^{-1})$ value for λ_c is preferred for long-term simulations ($O(10^3)$ periods).

For a given quadruplet, we choose k_1, k_2 and k_3 at the wavenumber grid points, and k_4 is naturally determined by (2.9). Unless otherwise specified, the action density $C(k_4)$ is obtained through bilinear interpolation (van Vledder 2006). When k_4 falls beyond the spectral grid, we assume

$$C(k_4) = \begin{cases} 0, & \text{for } k_4 < k_{min}, \\ C(k_{max}) \left(\frac{k_4}{k_{max}}\right)^{n/2-2}, & \text{for } k_4 > k_{max}, \end{cases} \quad (2.10)$$

where k_{min} and k_{max} are the minimum and maximum wavenumbers within in the spectral grid, and $n = -5$ is the prescribed high-frequency power law for frequency spectrum (i.e. $E(f) \propto f^n$).

2.1.3. Phase mixing

As noted in § 1, the GKE (2.3)–(2.5) is generally solved by assuming wave phases are initially completely uncorrelated, i.e. a cold start with $I(t = 0) = 0$ (GS13; AS18). As wave field evolves, the nonlinear four-wave interactions give rise to deviation from Gaussianity (Janssen 2003), resulting in non-zero fourth-order cumulant and, hence, non-zero $I(t)$. Some physical processes such as wave breaking (e.g. Babanin *et al.* 2010) may uncorrelate phases (i.e. phase re-mixing) at certain times. GS13 and GB16 suggested such effect could be incorporated in the GKE algorithm by restarting the GKE (setting $t = 0$) every N_{pm} characteristic wave periods (in terms of $T_{0,-1}$; appendix B) while keeping the action spectrum unchanged. As we show in the following, the phase re-mixing is also desired to suppress the numerical instability of the GKE for long-term simulations.

Two options for N_{pm} have been made available: N_{pm} can either be a fixed constant ($N_{pm} \sim O(10^2)$) or explicitly depend on the dominant breaking probability b_T by employing $N_{pm} = 1/b_T$ and

$$b_T = 85.1(\varepsilon_{p,w} - 0.055)^{2.33} \quad (2.11)$$

according to Babanin, Young & Banner (2001, their figure 12). Here $\varepsilon_{p,w}$ is the significant steepness of the spectral peak:

$$\varepsilon_{p,w} = 2 \left[\int_{0.7f_{p,w}}^{1.3f_{p,w}} E_w(f) df \right]^{1/2} k_{p,w}, \quad (2.12)$$

where $E_w(f)$ is the 1-D wave spectrum, $k_{p,w}$ and $f_{p,w}$ are the peak wavenumber and frequency, respectively. The subscript ‘w’ means these quantities are computed from wave spectrum $F(f, \theta)$ after filtration of swells. Following Bidlot (2001), we consider spectral components as wind seas if

$$\frac{c}{U_{10} \cos(\theta - \theta_u)} < \beta_w, \quad (2.13)$$

where $c = \omega/k$ is the phase velocity, $U_{10}(\theta_u)$ is the wind velocity (direction) 10 m above the sea surface, β_w is an empirical wind forcing parameter with $\beta_w \in [1.0, 2.0]$ used in the

literature (e.g. Janssen *et al.* 1989; Barstow *et al.* 2005). Here, by default, we have chosen $\beta_w = 1.2$.

2.1.4. Source term integration

Third-generation spectral wave models usually employ a semi-implicit or implicit integration scheme to calculate the change of action density ΔN in the time step Δt from source terms $S = S/\omega$:

$$\Delta N(k, \theta) = \frac{S(k, \theta)\Delta t}{1 - \epsilon D(k, \theta)\Delta t}, \tag{2.14}$$

where $D(k, \theta) = \partial S(k, \theta)/\partial N(k, \theta)$ is the diagonal term and $\epsilon = 1/2$ or 1 is the implicitness parameter (e.g. The WAMDI Group 1988; van Vledder 2006; Tolman 2013). Owing to the presence of the time integral $I(t)$ in (1.10) which explicitly depends on the history of the evolution of wave spectrum (in terms of the action product term $\mathcal{F}_{1,2,3,4}(\tau)$), it is challenging, if not impossible, to compute the diagonal term $D(k, \theta)$ for the GKE. To circumvent this problem, we adopt the explicit dynamic time-stepping scheme ($\epsilon = 0$) of Tolman (1992) for source term integration when S_{nl} is based on the GKE.

For a fixed global time step Δt_g , the source term integration is performed over a number of dynamic time steps Δt_d^i :

$$\left. \begin{aligned} \Delta t_d^i &= \min \left[\Delta t_g - \sum_{j=1}^{i-1} \Delta t_d^j, \min_{\forall \theta; f \leq f_{hf}} \left(\frac{\Delta N_{max}(k)}{|S(k, \theta)|} \right)^i \right], \\ \Delta t_d^i &= \max \left(\Delta t_d^i, \Delta t_{d,min} \right) \quad \text{and} \quad \sum \Delta t_d^i = \Delta t_g, \end{aligned} \right\} \tag{2.15}$$

where $\Delta N_{max}(k)$ is the maximum allowed change of action density per spectral bin per time step that is generally chosen as a certain fraction ($\sim 10\%$) of the Pierson–Moskowitz energy level, $\Delta t_{d,min}$ is a user-defined minimum dynamic time step, and $f_{hf} = N_{hf}/T_{0,-1}$ is the high-frequency limit of the prognostic region of the spectrum. The reader is referred to Tolman (1992) and WW3DG19 for more technical details of this explicit dynamic scheme. GB16 assumed $D(k, \theta) = 0$ but used the default implicit scheme ($\epsilon = 1$) in WW3. These two settings are apparently incompatible particularly when both S_{nl} and other terms (e.g. S_{in}, S_{ds}) are activated in the computations.

2.2. The JKE and HKE

We implement the JKE (1.7) under the framework of the GKE algorithm similarly as mentioned previously except that $R(\Delta\omega, t)$ is solved directly based on (1.8) and (1.9). Likewise, the phase mixing for the JKE is achieved by restarting it (setting $t = 0$) periodically. The HKE (1.3) is computed based on the Webb–Resio–Tracy (WRT) approach (Webb 1978; Tracy & Resio 1982; Resio & Perrie 1991; van Vledder 2006) with an implicit ($\epsilon = 1$) dynamic integration scheme (Tolman 1992).

3. Parameter settings

As described in the previous section, two parameters for the GKE and JKE algorithms remain undefined: the quasi-resonant cut-off factor λ_c in (2.9) and the number of wave periods for phase mixing N_{pm} . A single-grid-point, duration-limited wave growth experiment under $U_{10} = 20 \text{ m s}^{-1}$ (Tolman 2013, his test_01) is conducted here to investigate the impact of these parameters on model results. The initial condition selected

is a JONSWAP spectrum (Hasselmann *et al.* 1973) with a peak frequency of 0.25 Hz and significant wave height $H_s \simeq 0.7$ m (the high-frequency energy level $\alpha = 0.0081$ and peak enhancement factor $\gamma = 2$; appendix B). We choose the source term package ST6 (Rogers, Babanin & Wang 2012; Zieger *et al.* 2015; Liu *et al.* 2019) for estimating the wind input and wave breaking terms (S_{in} , S_{ds}). Other model settings can be found in table 2.

Considering (i) that wind blows steadily in this duration-limited case and, hence, the wave field evolves slowly and (ii) that wave spectra are sufficiently broad and, thus, non-resonant interactions contribute little to the development of wind waves, we expect that the three kinetic equations (HKE, JKE and GKE) should yield essentially the same evolution of wave spectrum (Annenkov & Shrira 2015, 2016). Using the HKE-based results as the baseline reference, we quantify the accuracy of the JKE and GKE simulations with the following metrics:

$$\epsilon_x = \sqrt{\frac{1}{N} \sum_N \left(\frac{x - x_H}{x_H} \right)^2}, \tag{3.1}$$

$$\epsilon_T = \sum_{H_s, \dots, \sigma_\theta} \epsilon_x, \tag{3.2}$$

where x and x_H represent integral wave parameters from the GKE/JKE and HKE runs, respectively. Six wave parameters are selected, including wave height H_s , peak frequency f_p , Goda’s spectral narrowness Q_p , angular spreading σ_θ , Donelan’s high-frequency energy level α_D and peak enhancement factor γ_D (appendix B). The root-mean-square (r.m.s.) difference ϵ_x (3.1) defined for each wave parameter is then combined into a single difference metric ϵ_T (3.2).

During our numerical experiments, it was quickly found that the GKE and JKE simulations without phase mixing ($N_{pm} = \infty$) will become numerically unstable at large times and eventually deviate significantly from the HKE growth curve (figure 14). AS18 also demonstrated that their GKE-simulated spectra present noticeable high-frequency noise after a few hundreds of wave periods of integration (their figure 6). It is presumed that this numerical instability results from the rapidly oscillating terms present in the GKE/JKE ($I(t)$ or $R(\Delta\omega, t)$). We found, however, remixing phases periodically can effectively remove all high-frequency noise and stabilize the GKE/JKE integration, generating a wave growth curve close to that for the HKE (figure 14).

Figure 2 shows the total difference ϵ_T of the GKE results relative to the HKE counterparts as a function of N_{pm} and λ_c , where the GKE is solved based on (2.7). For λ_c fixed at 0.1, the GKE presents minimum ϵ_T (closest to the HKE) in the vicinity of $N_{pm} = 100$ (figure 2a). For N_{pm} fixed, ϵ_T drops rapidly as λ_c increases from 0.01 to 0.1 but changes marginally for larger cut-off values (figure 2b), which again suggests four-wave interactions very far from resonance plays a very limited role in the development of wind waves. It should be noted that the total number of unique quadruplets N_q (appendix A) and, hence, the computational expense of the GKE scale linearly with λ_c (red triangles in figure 2b). Under U_{10} of 20 m s⁻¹, the dominant breaking probability b_T according to (2.11) decreases from 15 % for very young wind seas ($t \sim 2$ h) to almost zero for mature, nearly fully developed wave conditions (figure 2c). The experiment with $N_{pm} = 1/b_T$ corresponds to an ϵ_T of 26 %, falling in between differences for $N_{pm} = 10$ and $N_{pm} = 30$. Difference metrics for the JKE are practically the same and, thus, are not reproduced here.

The evolution of six selected integral wave parameters simulated by all the three kinetic equations is presented in figure 3, where λ_c and N_{pm} are fixed at 0.1 and 100, respectively. When (2.7) is employed (labelled as $\mathcal{D}_K = 0$), the GKE and JKE are in

Experiment	f_1 (Hz)	δ	N_f	$\Delta\theta$ ($^\circ$)	N_{hf}	λ_c	N_{pm}	N_q	U_{10} (m s^{-1})	c_i (%)	S_{in}, S_{ds}	Section
Duration-limited growth	0.04	1.07	45	10	6	[0.01, 0.25]	[10, 1000]	$[4, 90] \times 10^6$	20	/	ST6	3
Adiabatic-Gaussian	—	1.053	50	5	∞	0.1	100, ∞	6×10^8	/	/	/	4
Turing winds	—	1.07	45	10	6	—	100	4×10^7	10	/	ST6	5
Ice-coupled	—	—	—	—	∞	—	—	—	20	50	—	6

Table 2. The model set-up for different wave experiments, including the frequency grid $f_i = \delta^{i-1} f_1$, $i = 1, \dots, N_f$, directional bin size $\Delta\theta$, high-frequency extent of the prognostic region N_{hf} , quasi-resonant cut-off factor λ_c , number of wave periods for phase mixing N_{pm} , total number of unique quadruplets N_q , external wind and ice forcing (U_{10} , ice concentration c_i) and source term package for S_{in} , S_{ds} . The global (source term) integration time step Δt_g ($\Delta t_{d,min}$) used is 10 (1) s. $N_{hf} = \infty$ means the high-frequency tail evolves freely without any prescribed slope; $N_{pm} = \infty$ denotes the GKE/JKE is solved without phase mixing.

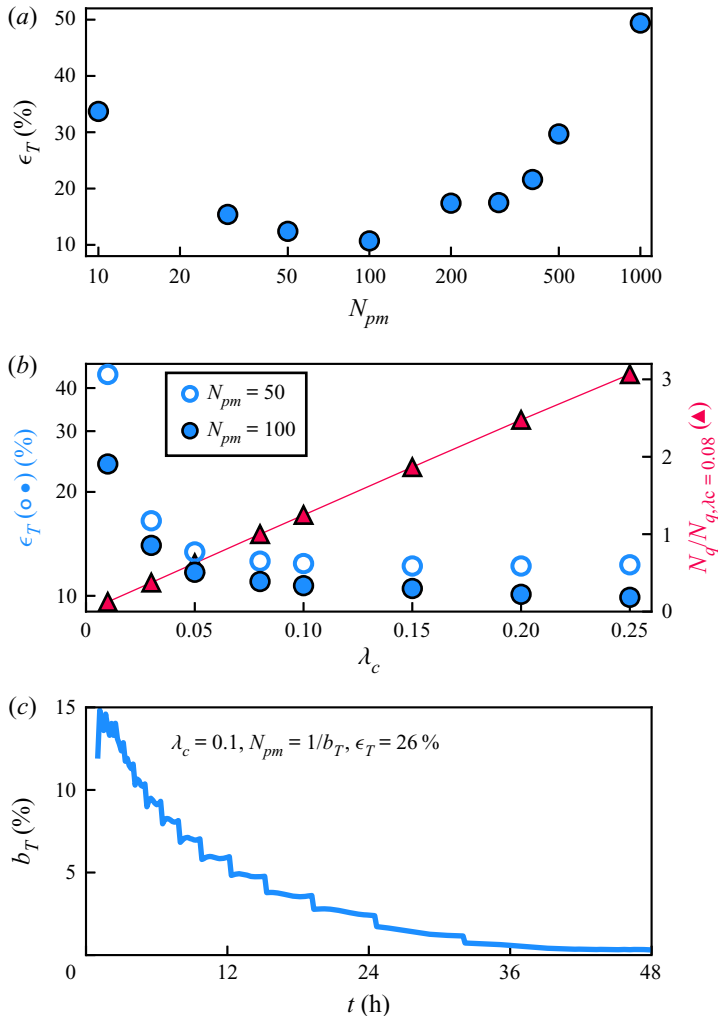


Figure 2. Total difference ϵ_T of the GKE results (based on (2.7)) as a function of (a) the number of periods for phase mixing N_{pm} ($\lambda_c = 0.1$) and (b) the quasi-resonant cut-off factor λ_c (empty and full circles: $N_{pm} = 50$ and 100). Red triangles in (b) show the total number of unique quartets N_q (normalized by $N_{q,\lambda_c=0.08}$). (c) Evolution of the dominant breaking probability b_T (2.11) with time. The experiment with $N_{pm} = 1/b_T$ and $\lambda_c = 0.1$ yields an ϵ_T of 26%.

excellent agreement with the HKE except that the angular spreading σ_θ from the formers are slightly lower (figure 3f; see also figure 2 of Annenkov & Shrira 2016). Wave spectra from the GKE based on (2.6) (labelled as $\mathcal{D}_K = 1$), as used by GB16, are remarkably broader in both frequency and directional spaces, evidenced by the clearly underestimated spectral peakedness (Q_p and γ_D ; figure 3c,e) and overestimated spreading (σ_θ ; figure 3f). Meanwhile, the high-frequency energy level α_D when using (2.6) is considerably higher (figure 3d). As a comparison, the total differences ϵ_T for the GKE with (2.6) and (2.7) are 142% and 11%, respectively. Figure 3 (thin yellow and purple lines) also clearly displays that spectral peakedness γ_D is more sensitive than H_s and f_p to the frequency of phase mixing.

It is further noted that (2.6) tends to suppress the bimodality of short waves (e.g. Romero & Melville 2010; Liu *et al.* 2019), as demonstrated in figure 4 where the normalized angular

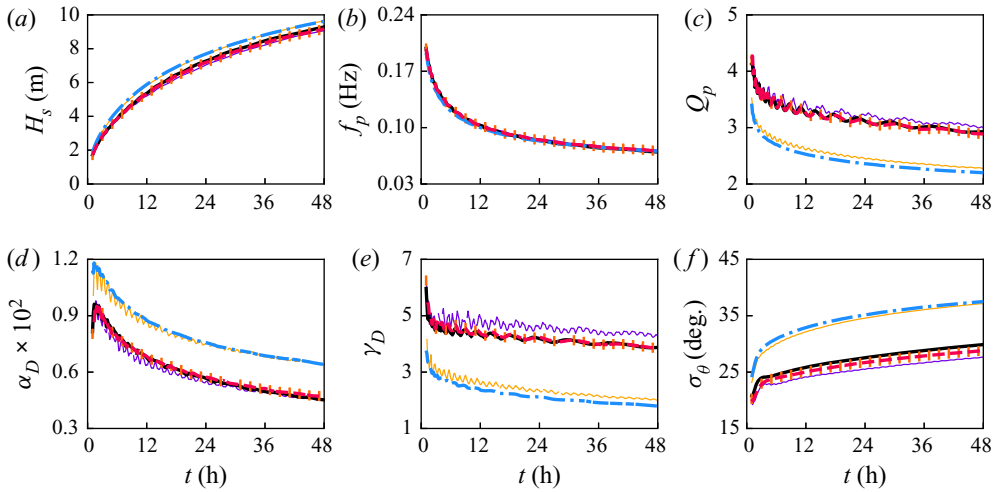


Figure 3. Evolution in time of (a) significant wave height H_s , (b) peak frequency f_p , (c) Goda’s spectral narrowness Q_p , (d) Donelan’s high-frequency energy level α_D , (e) peak enhancement factor γ_D and (f) angular spreading σ_θ according to the (black solid line) HKE, (blue dash-dotted line) GKE ($\mathcal{D}_\kappa = 1$; (2.6)), (red dashed line) GKE ($\mathcal{D}_\kappa = 0$; (2.7)) and (orange ‘I’) JKE ($\mathcal{D}_\kappa = 0$; (2.7)) in the duration-limited test. Here $\lambda_c = 0.1$ and $N_{pm} = 100$ are chosen for the GKE and JKE simulations. Model spectra are selected at 10 min interval starting with 1 h forecast. To illustrate the impact of phase mixing, the GKE results with $N_{pm} = 500$ are also shown: thin yellow line (2.6) and thin purple line (2.7).

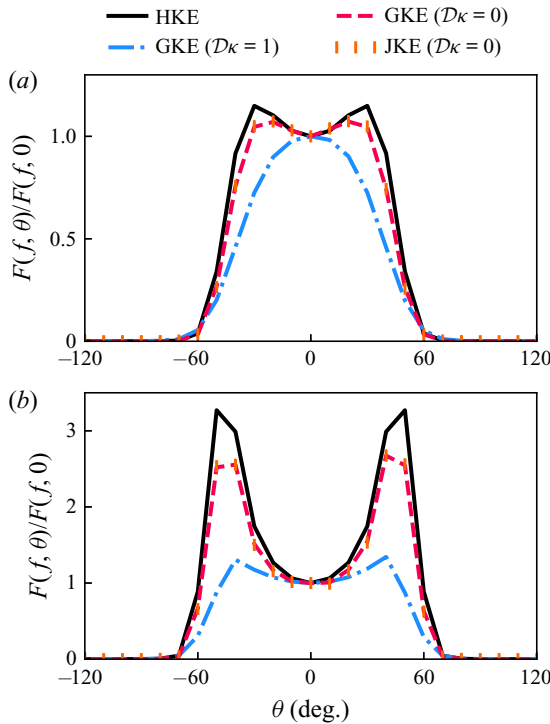


Figure 4. Comparison of the normalized angular distribution, $F(f, \theta)/F(f, 0)$, of wave spectrum after 8 h of model integration: (a) $f = 2f_p$; (b) $f = 3f_p$. Here $\theta = 0^\circ$ denotes the wind direction and the corresponding wave age is $U_{10}/c_p \simeq 1.5$ ($c_p/u_* \simeq 15$). Legend as in figure 3.

distribution $F(f, \theta)/F(f, 0)$ for the wave spectrum after ~ 8 h of model integration (the corresponding inverse wave age $U_{10}/c_p \simeq 1.5$) is presented. Here $\theta = 0^\circ$ corresponds to the wind direction and hence the dominant wave direction. Clearly, at $2f_p$, the GKE with (2.6) fails to reproduce the bimodal distribution (figure 4a); at $3f_p$, its predicted bimodal lobes are much shallower than those for the GKE/JKE based on (2.7) and for the HKE (figure 4b).

Considering the results above, the default settings in WW3 for the GKE and JKE are defined by (2.7), $\lambda_c = 0.1$ and $N_{pm} = 100$. All these parameters, however, can be easily redefined by the user through namelist variables (WW3DG19).

4. Adiabatic evolution of a Gaussian wave spectrum

In this section, we investigate the short-term ($O(10^2)$ wave periods), adiabatic evolution of an initially Gaussian wave spectrum. Here by ‘adiabatic’ we mean physical processes except for the four-wave interactions are neglected ($S_{in} = S_{ds} = 0$). The initial 2-D Gaussian spectrum $F(f, \theta) = E(f)D(\theta)$ is specified by

$$E(f) = \frac{\varepsilon^2 g^2}{4(2\pi)^{9/2} f_p^5 \sigma_g} \exp \left[\frac{-(f - f_p)^2}{2\sigma_g^2 f_p^2} \right], \quad (4.1)$$

where $\varepsilon = H_s k_p / 2$ is the wave steepness, σ_g controls the spectral width and the angular spreading function $D(\theta)$ follows the $\cos^N \theta$ model (Holthuijsen 2007):

$$D(\theta) = \begin{cases} \frac{1}{\sqrt{\pi}} \frac{\Gamma(N/2 + 1)}{\Gamma(N/2 + 1/2)} \cos^N(\theta - \theta_w), & \text{for } |\theta - \theta_w| \leq 90^\circ, \\ 0, & \text{for } |\theta - \theta_w| > 90^\circ, \end{cases} \quad (4.2)$$

where Γ is the Gamma function and θ_w is the dominant wave direction.

The initial wave field considered here is defined with $\varepsilon = 0.2$, $\sigma_g = 0.1$, $N = 90$ and $f_p = 0.1$ Hz (black line in figure 5), featuring a Benjamin–Feir index $\text{BFI} = \varepsilon / (2\Delta f / f_p) = 0.86 > 1/\sqrt{2}$, where Δf is the half-width at the half-maximum of $E(f)$ (Janssen 2003; Onorato *et al.* 2006; Xiao *et al.* 2013). A relatively high-resolution (f, θ) grid is used to better resolve this directionally narrow spectrum ($\delta = 1.053$, $\Delta\theta = 5^\circ$; table 2). For this short-term evolution, phase mixing practically makes very little difference in the GKE/JKE-based results (figure 6).

Figure 5 presents the computed wave spectra at $t = 50, 100$ and 200 wave periods according to distinct kinetic equations. The evolution in time of integral wave parameters over 300 periods is illustrated in figure 6, complemented by the spectrogram for the first 150 periods displayed in figure 7. The consistent features revealed by three equations are the noticeable downshifting of the spectral peak (figures 6b and 7), remarkable angular broadening (figure 6e) and the gradual development of the f^{-4} high-frequency decay (figures 5 and 7; wave energy starts accumulating at the high-frequency tail at $t = 200$ periods because of the lack of dissipation). Similar results have been reported by Onorato *et al.* (2002) and Dysthe *et al.* (2003), among others.

The growth of the rear face of the spectrum ($f > f_p$), initially severely truncated and eventually f^{-4} sloped owing to the shape-stabilizing role of the four-wave interactions (Young & van Vledder 1993), differs noticeably across distinct kinetic equations. It is seen that the GKE leads to the fastest growth of the tail, closely followed by the JKE with the HKE measurably falling behind (figures 5 and 6d). Meanwhile, wave spectra from

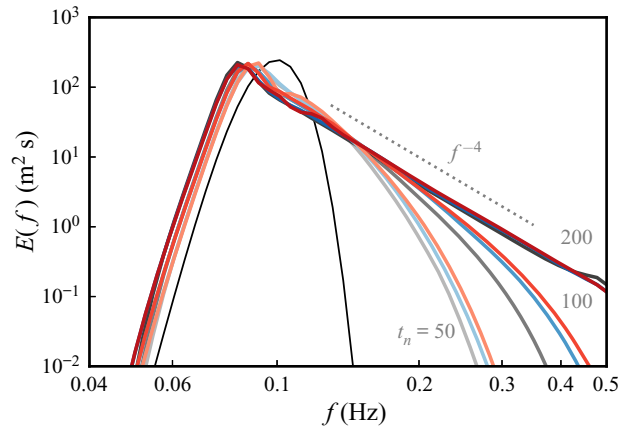


Figure 5. Evolution in time of wave spectrum $E(f)$ according to the (grey lines) HKE, (blue lines) JKE ($N_{pm} = \infty$) and (red lines) GKE ($N_{pm} = \infty$). Wave spectra shown are at time $t_n = t/T_p = 50, 100, 200$ periods. The black line represents the initial Gaussian spectrum defined by (4.1) and (4.2) with $\varepsilon = 0.2, \sigma_g = 0.1, N = 90$ and $f_p = 0.1$ Hz. The grey dotted line represents the f^{-4} reference slope.

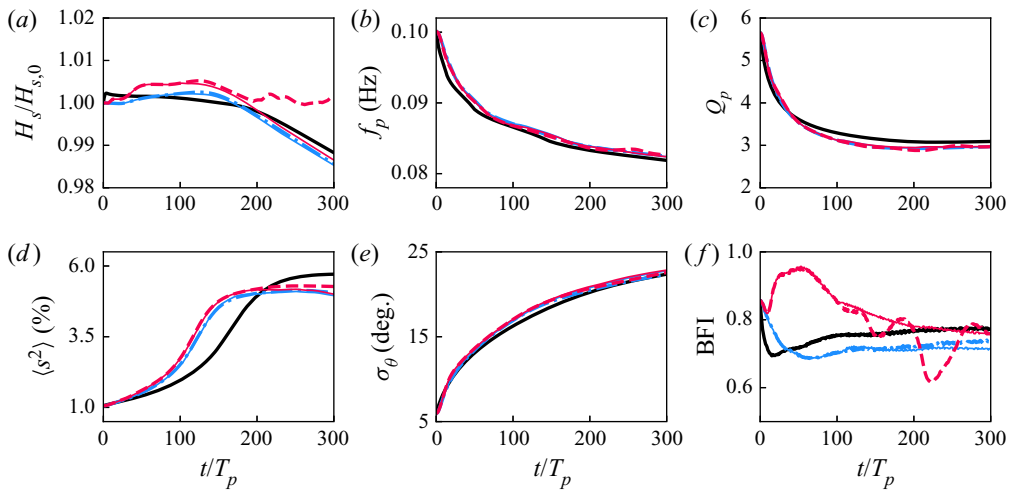


Figure 6. Short-term evolution of the (a) significant wave height (normalized by the initial value) $H_s/H_{s,0}$, (b) peak wave frequency f_p , (c) Goda's spectral narrowness Q_p , (d) mean square slope $\langle s^2 \rangle$, (e) angular spreading σ_θ and (f) BFI according to the (black solid line) HKE, (blue lines) JKE and (red lines) GKE. The thick and thin coloured lines refer to the corresponding JKE/GKE solved without and with phase mixing ($N_{pm} = \infty, 100$), respectively. Model spectra are selected at 10 s interval.

the JKE and GKE are slightly wider in both frequency and directional spaces than those from the HKE (figures 6c,e and 7), qualitatively similar to results reported in Annenkov & Shrira (2018, 2019). At $t > 200$ periods, the f^{-4} slope is well formed at the rear face of the spectrum (figure 5), then $\langle s^2 \rangle$ from all the equations gets closer (figure 6d). The residual differences in $\langle s^2 \rangle$ are likely attributed to differences in the numerical algorithms. Wave energy from all the kinetic equations is not perfectly conserved (figure 6a) owing to the defects in our numerical approach and the finite extent of the spectral domain (e.g. Resio & Perrie 1991; Rogers *et al.* 2012). Both JKE and HKE produce a minimal BFI

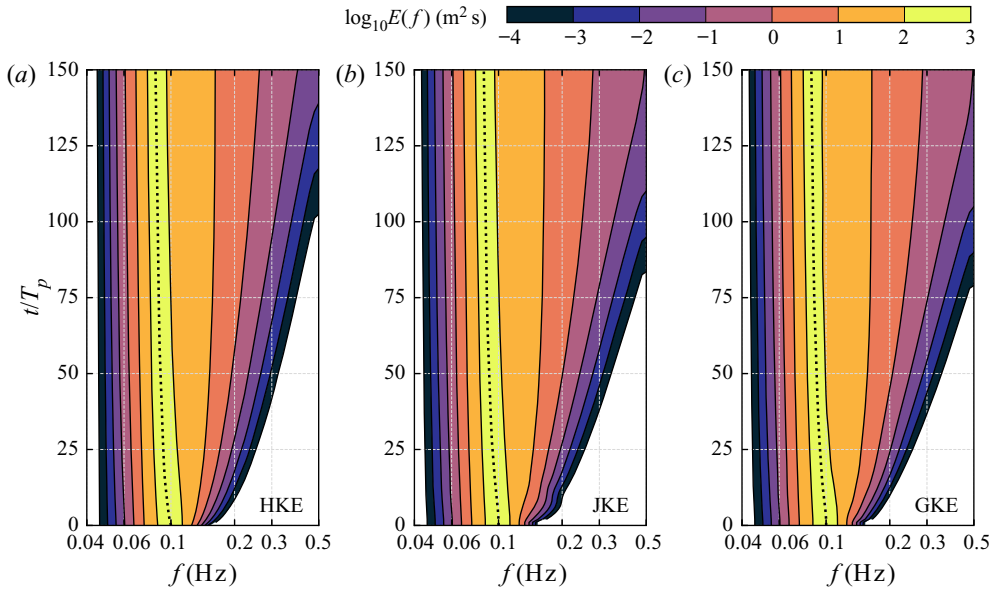


Figure 7. Spectrogram of the simulated wave fields according to the (a) HKE, (b) JKE ($N_{pm} = \infty$) and (c) GKE ($N_{pm} = \infty$). The wave spectrum $E(f)$ is shown in a logarithmic scale, and the dotted line highlights the location of peak frequency f_p .

within the first 100 periods of model integration (figure 6f), whereas the GKE-based BFI maximizes at $t \sim 60$ periods, and then declines with time. This is primarily because that the GKE-simulated $E(f)$ is not fully smooth at $f > f_p$ for $t < 75$ periods (a plateau present at $f \sim 1.2f_p$; figure 5), resulting in narrower spectral peak width Δf and accordingly larger BFI. As one would expect for a freely evolving wave system, the directional BFI (i.e. the index including the effect of angular spreading; Xiao *et al.* 2013) from all the equations decreases with time (not shown).

It has long been argued that the HKE, as prescribed by its formulation, predicts wave fields evolve on a slow, ‘kinetic’ time scale $O(1/\varepsilon^4 \omega_0)$; whereas the GKE and JKE introduce the effect of quasi-resonant four-wave interactions, thereby being capable of advancing evolution on a fast, ‘dynamic’ time scale $O(\varepsilon^{-2} \omega_0)$, also known as Benjamin–Feir instability time scale or modulational instability time scale (Hasselmann 1962; Dysthe *et al.* 2003; Janssen 2003; Annenkov & Shrira 2006, 2009, GS13, among others). A striking outcome identified in figures 5–7 is that the three equations initially operate at the same ‘dynamic’ time scale ($\varepsilon^{-2} = 25$ periods) for the spectral peak downshift and angular broadening. Although counter-intuitive, comparable results were also reported by AS18, showing that the HKE, GKE and Zakharov equations yield very close evolution of integral wave parameters for an initially unstable wave spectrum subject to strong modulational instability (their figure 8; see our § 8 for further discussion regarding these results).

The average growth rate of wave spectrum over the first 100 periods as a result of the nonlinear transfer, defined as

$$\langle S_{nl}(f) \rangle = \frac{E(f, t = 100T_p) - E(f, t = 0)}{100T_p}, \quad (4.3)$$

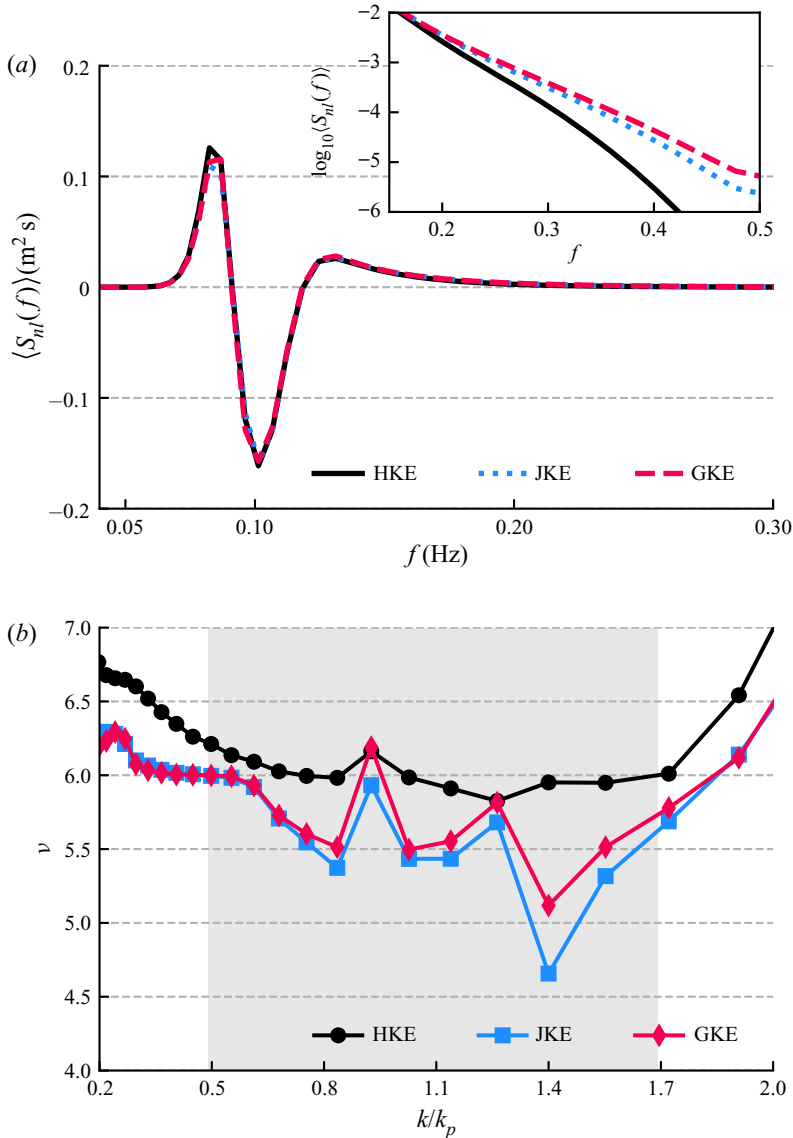


Figure 8. (a) The average growth rate $\langle S_{nl}(f) \rangle$ over the first 100 periods as a function of frequency f . The inset shows $\langle S_{nl}(f) \rangle$ in a logarithmic scale for high frequencies. (b) The exponent ν for the scaling of $S_{nl}^{max} \sim \varepsilon^\nu$ as a function of k/k_p . The shaded area highlights the energy-containing range of the initial Gaussian spectrum, as approximated by $k/k_p \sim (1 \pm 3\sigma_g)^2$. Black/blue/red line: HKE/JKE/GKE. The latter two equations are solved without phase mixing ($N_{pm} = \infty$).

is plotted in figure 8(a). Here $\langle S_{nl} \rangle$ arising from three kinetic equations is nearly the same except for the spectral tail ($f > 3f_p$), exhibiting a positive lobe below f_p , a negative lobe in the vicinity of f_p and another positive lobe at higher frequencies. AS18 suggested that the scaling of growth rate S_{nl} with wave steepness ε , rather than the growth rate itself, could be a good indicator to sort out different kinetic equations. The authors found that the HKE corresponds to $S_{nl}^{max}(f) \sim \varepsilon^6$, where $S_{nl}^{max}(f)$ was the maximal growth rate attained in their simulations; their direct simulations based on the Zakharov equation favours

$S_{nl}^{max}(f) \sim \varepsilon^4$ (see also Annenkov & Shrira 2009) and the GKE features a scaling in between, i.e. $S_{nl}^{max}(f) \sim \varepsilon^{5 \sim 5.5}$. We checked this idea as well by conducting simulations of multiple Gaussian spectra with various steepness ($\varepsilon = 0.035, 0.05, 0.07, 0.10, 0.14, 0.2$) while keeping other parameters (e.g. σ_g, f_p) unchanged. Following AS18, a first-degree polynomial fit is performed onto the estimated $S_{nl}^{max}(f)$ at each frequency by adopting

$$\log S_{nl}^{max}(f) = \nu(f) \log \varepsilon + \beta, \quad (4.4)$$

and the resulting exponent ν is illustrated in figure 8(b). Consistent with AS18, for most of the energy-containing frequency range (shaded region in figure 8b), we have $\nu \sim 6$ and $\nu \sim 5.5$ for the HKE and GKE, respectively; the JKE yields a comparable scaling to the GKE.

5. Directional response of waves to turning winds

The situation that wind changes rapidly, quite often occurring under tropical cyclones or strong frontal systems, represents an interesting case where the fast evolution of wave spectrum may take place and, therefore, where the three kinetic equations may behave dissimilarly. Field observations and numerical simulations of the response of wind waves to turning winds have been conducted thoroughly in the literature, and the reader is referred to van Vledder & Holthuijsen (1993, hereafter VH93) for reviews of this topic.

A consistent picture of the directional relaxation of a wind–sea spectrum to abrupt changes in wind direction is that the time scale τ for the turning of mean wave direction θ_w (appendix B) toward the new wind direction θ_u , usually defined by the following relaxation model (e.g. VH93)

$$\frac{\partial \theta_w}{\partial t} = \frac{1}{\tau} \sin(\theta_u - \theta_w), \quad (5.1)$$

depends on the stage of development of the wave field with young waves featuring short time scales.

Here, we simulate these spectral responses with the three different kinetic equations. A constant U_{10} of 10 m s^{-1} is imposed, and the initial JONSWAP spectrum is defined with $f_p = 0.5 \text{ Hz}$ and $H_s \sim 0.19 \text{ m}$. Other model attributes are the same as the duration-limited growth test described in § 3 (table 2). Following VH93, a sudden wind shift is introduced at $t = 3 \text{ h}$ when the dimensionless peak frequency f_p approximately reaches $2f_{PM}$, where $f_{PM} = 5.6 \times 10^{-3} g/u_*$ is the fully developed Pierson–Moskowitz peak frequency (Komen, Hasselmann & Hasselmann 1984) and u_* is the friction velocity. The spectral response time scale τ can be estimated from model results based on a finite-difference version of (5.1):

$$\tau(t_j) = \frac{t_{j+1} - t_{j-1}}{\theta_{w,j+1} - \theta_{w,j-1}} \sin(\theta_{u,j} - \theta_{w,j}), \quad (5.2)$$

where the subscript ‘ j ’ is the local counter for the time interval at which model spectra are stored (15 min selected here). Similar to VH93, five-point moving averages over the time series were used to reduce scatter in the estimated τ .

Figure 9 presents the dimensionless $\tau_* = g\tau/u_*$ as a function of the dimensionless frequency $\nu_* = f_p u_*/g$ for wind shift θ_u of $30^\circ, 45^\circ, 60^\circ$ and 90° according to different kinetic equations. Observations and simulations reported by VH93 are also shown as references. Our HKE-based results (grey markers) show that: (i) τ_* increases as wave develops ($\nu_* \downarrow$), consistent with previous studies; (ii) τ_* is noticeably dependent on wind shift with waves turning faster for lower θ_u ; and (iii) the average time scale over different

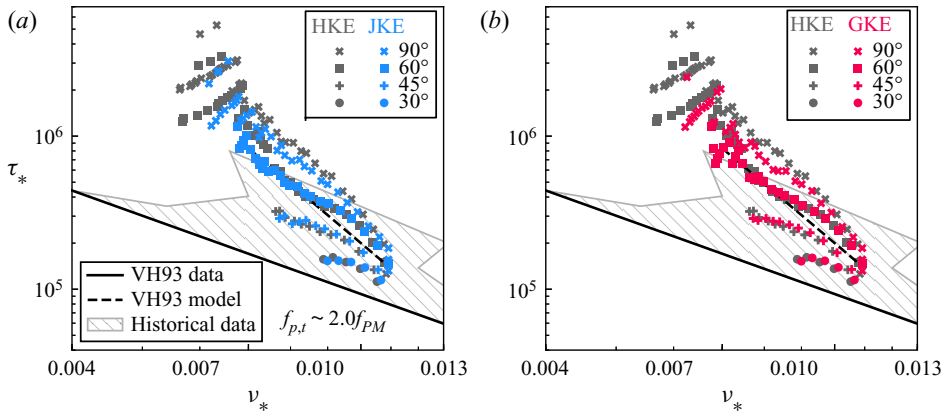


Figure 9. Dimensionless response time scale $\tau_* = g\tau/u_*$ as a function of dimensionless peak frequency $\nu_* = f_p u_*/g$ (figure adapted from figure 12 of [VH93](#)): (a) (grey) HKE versus (blue) JKE; (b) (grey) HKE versus (red) GKE; ‘ \times ’, ‘ \blacksquare ’, ‘ \oplus ’, ‘ \bullet ’ for the directional shift θ_u of 30°, 45°, 60°, 90°. Black solid and dashed lines represent the relations derived by [VH93](#) based on their observations ($\tau_* = 37\nu_*^{-1.7}$) and EXACT-NL simulations ($\tau_* = 0.002\nu_*^{-4.0}$), respectively. The hatched area illustrates the published data summarized by [VH93](#) in their figure 3. The density of markers for model results has been reduced for clarity.

wind shifts as yielded by the state-of-the-art physics for S_{in} and S_{ds} (i.e. ST6) does not deviate significantly from the model results presented in [VH93](#) (black dashed line in [figure 9](#)), where the authors also used the HKE for S_{nl} (EXACT-NL) but with different wind input and wave breaking physics ([Komen *et al.* 1984](#)). For old wind seas (low ν_*), the simulated directional relaxation is considerably slower than observations from [VH93](#). The JKE and GKE (blue and red markers) are not dissimilar to the HKE. Although unexpected, this is, however, in line with findings from [Annenkov & Shrira \(2015\)](#) who found the HKE and GKE produce nearly identical results during a squall event (sharp increase in wind speed). The significant differences between distinct kinetic equations as observed by [GB16](#) for comparable situations are primarily attributed to the two numerical flaws (discretization and source term integration) in their computations.

6. Ice-coupled waves

Numerical simulations of the Gaussian wave spectrum presented in § 4 indicate when the spectral tail is significantly truncated, quasi-resonant four-wave interactions may lead to faster development of the f^{-4} high-frequency decay. Such unusual spectral shape, however, rarely exists in real oceans except for ice-coupled waves.

Field experiments suggest that when ocean waves propagate into ice fields, wave energy decays exponentially with distance, according to the following form (e.g. [Wadhams *et al.* 1986](#))

$$\frac{1}{F(f, x)} \frac{dF(f, x)}{dx} = -\alpha_i(f, \mathcal{I}), \tag{6.1}$$

where $F(f, x)$ is the 1-D wave spectrum at a penetration x , α_i is the spatial attenuation rate of wave energy, depending on wave frequency f and ice parameters \mathcal{I} . For given ice conditions, α_i generally increases with increasing wave frequency ([figure 10](#)). Consequently, wave spectra collected at ice-infested seas usually have heavily attenuated tails (see, e.g., figure 6 of [Rogers *et al.* 2016](#)). It may, thus, be inspiring to explore the growth of ice-coupled waves with different kinetic equations.

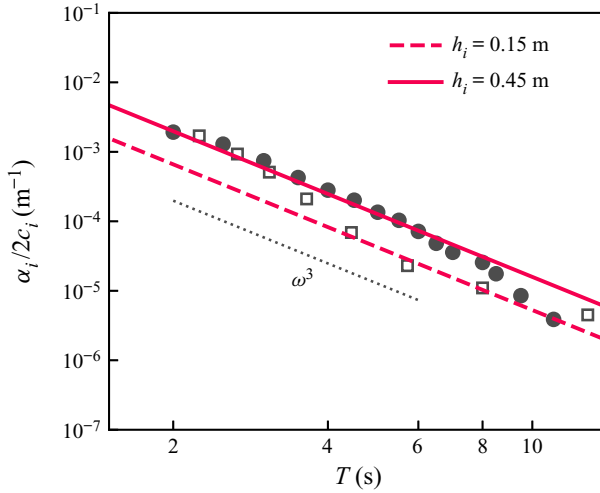


Figure 10. Attenuation rate of ice-coupled waves $\alpha_i/2c_i$ as a function of wave period T . Filled circles ● and empty squares □ represent observations from Cheng *et al.* (2017) and Rogers, Meylan & Kohout (2018) collected under an Arctic storm event. Dashed and solid red lines show estimations by (6.3) with $\eta = 14 \text{ kg m}^{-3} \text{ s}^{-1}$, $h_i = 0.15$ and 0.45 m, respectively (figure adapted from figure 10 of Liu *et al.* 2020).

In order to simulate ice-coupled wave spectra, the action balance equation (1.1) is conventionally rewritten as (Masson & Leblond 1989)

$$\frac{dN}{dt} = \frac{(1 - c_i)(S_{in} + S_{ds}) + S_{nl} + S_{ice}}{\omega}, \tag{6.2}$$

where c_i is sea ice concentration, the wind input and wave breaking terms are reduced by a factor $(1 - c_i)$ and S_{nl} is left unchanged (Polnikov & Lavrenov 2007). The newly included S_{ice} term represents the impact of sea ice on wave energy. Although parameterizations of S_{ice} available in the literature are rather diverse (e.g. Rogers *et al.* 2016; Liu *et al.* 2020, see their table 1), here we select the viscous ice model of Meylan *et al.* (2018) and the corresponding S_{ice} term is given by (Liu *et al.* 2020, IC5 in WW3):

$$S_{ice}(k, \theta) = -c_g \underbrace{2c_i \frac{\eta h_i}{\rho_w g^2}}_{\alpha_i} \omega^3 F(k, \theta), \tag{6.3}$$

where c_g is the open-water group velocity (assuming no change in the dispersion relation), ρ_w is the density of water, h_i is the ice cover thickness and η (in $\text{kg m}^{-3} \text{ s}^{-1}$) is an empirical viscous parameter. It follows from (6.3) that the ice-induced wave decay scales linearly with h_i and is proportional to the frequency cubed (figure 10).

In the following simulations, we have arbitrarily chosen $\eta = 14 \text{ kg m}^{-3} \text{ s}^{-1}$ and $c_i = 50 \%$, largely following Liu *et al.* (2020) who have fit (6.3) to field wave measurements collected under a stormy event in the Arctic marginal ice zone with the same value of η (figure 10). Two ice thicknesses (0.15 and 0.45 m) were considered, signifying different strengths of the ice-induced wave decay. Other model settings (table 2) are practically the same as in the open-water, duration-limited wave growth test (§ 3).

Experiments with h_i of 0.15 m prove no differences in model results by three different equations (not shown). When the ice-induced attenuation becomes stronger ($h_i = 0.45$ m), however, the GKE and JKE (with $N_{pm} = 100$) produce remarkably faster wave growth

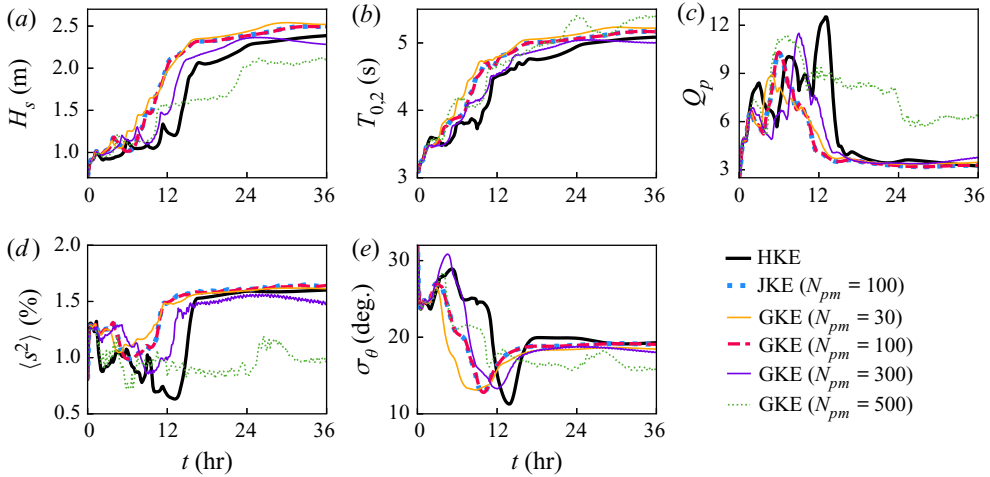


Figure 11. Evolution in time of (a) significant wave height H_s , (b) wave period $T_{0,2}$, (c) Goda's spectral narrowness Q_p , (d) mean square slope $\langle s^2 \rangle$, (e) angular spreading σ_θ according to the (black solid line) HKE, (blue dotted line) JKE ($N_{pm} = 100$) and (red dashed line) GKE ($N_{pm} = 100$) in the ice-coupled test ($h_i = 0.45$ m). Model spectra are selected at 10 min interval. The GKE results with $N_{pm} = 30, 300, 500$ (thin coloured lines) are also presented to illustrate the noticeable effect of phase mixing in this case.

than the HKE, as evident from figure 11. In this case, the growth curves are less smooth, particularly for the first 12 h. During 6–18 h of model integration, wave height H_s and wave period $T_{0,2}$ from the GKE/JKE are significantly higher than the HKE-based values, but eventually all the kinetic equations reach similar quasi-equilibrium states.

Inspection of wave spectra given in figure 12 reveals more complexity of the development of waves in this specific ice-coupled regime. Starting from the initial JONSWAP spectrum with minor energy ($H_s \simeq 0.7$ m, $f_p = 0.25$ Hz), wave grows due to the net balance of all the physical processes involved. At $t = 1$ h, the rear face of spectrum, particularly for $f < 0.4$ Hz, is apparently attenuated by ice; meanwhile, the wind input of ST6 (Donelan *et al.* 2006), being different from traditional parameterizations, injects more energy at high frequencies (see figure 4 of Zieger *et al.* 2015) and creates a secondary peak around $2f_p$. The nonlinear transfer will regard this secondary peak as a perturbation and work to smooth it out (Resio & Perrie 1991; Young & van Vledder 1993). These processes compete with each other and determine the underlying spectral shape. The secondary peak persists throughout 1–12 h in the HKE run and spectra at 6 and 12 h are noticeably noisy (figure 12a). Six hours later ($t \geq 18$ h), the spectrum turns into a smooth form with an evidently dissipated tail (orange and red lines in figure 12a). Wave spectra from the GKE run ($N_{pm} = 100$) get rid of the secondary peak at an earlier time ($t \sim 6$ h; figure 12c), facilitating the subsequent rapid growth over the next 12 h (figure 11).

Unlike the open-water, duration-limited wave growth test (figure 3), we found that the GKE simulations here are appreciably sensitive to the frequency of phase mixing. For $N_{pm} \in [30, 300]$, the more frequently wave phases are remixed, the earlier the wave spectrum becomes smooth (figure 12b,c), and accordingly the earlier the rapid growth (during which H_s roughly increases from 1 to 2 m) takes place (figure 11). When $N_{pm} = 500$, the numerical instability of the GKE is not well suppressed, as manifested by the severely saw-like spectral shape (even on the forward face) at $t = 36$ h (not shown). The corresponding wave parameters (green dotted line in figure 11) also markedly deviate from those for the HKE and other GKE runs (i.e. with lower N_{pm}), particularly for $t > 12$ h.

Kinetic equations in a third-generation spectral wave model

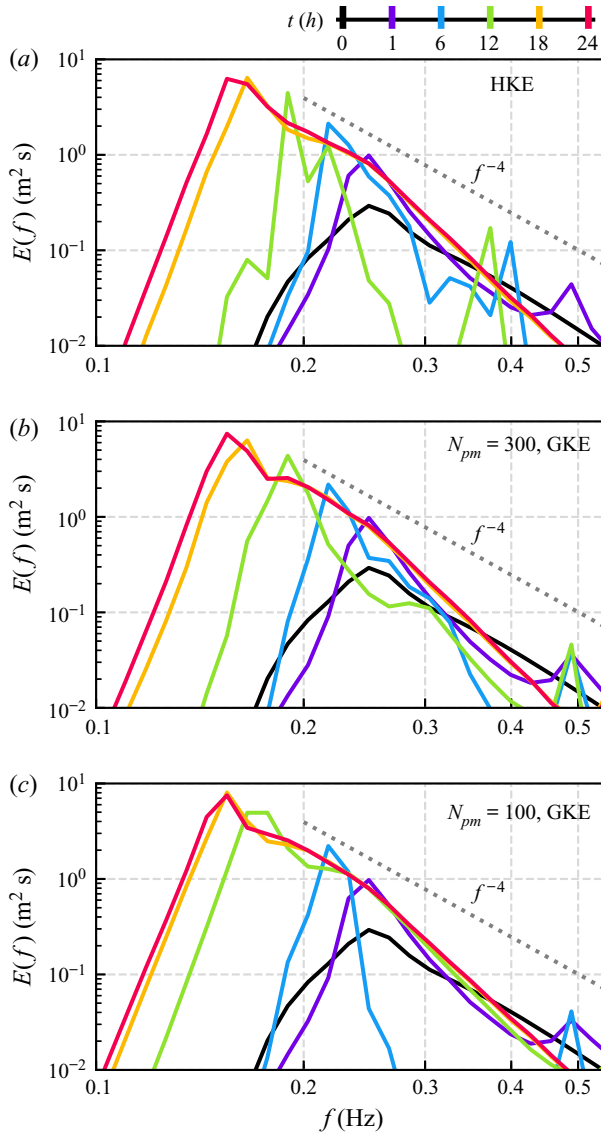


Figure 12. Development of wave spectrum $E(f)$ with time according to (a) the HKE, (b) the GKE ($N_{pm} = 300$) and (c) the GKE ($N_{pm} = 30$) in the ice-coupled test. For clarity, only spectra at $t = 0, 1, 6, 12, 18$ and 24 h are displayed. The reference slope proportional to f^{-4} is shown as the grey dotted line.

It is worth mentioning that the case presented here is unique and uncommon. All the unusual preconditions (e.g. ice coupling, unconventional wind input term and non-smooth spectra shape) coincidentally lead to different growth curves by three equations. It is thus less than definite to conclude that the fast evolution, as hypothesized by the GKE, is robustly confirmed for 2-D spectrum here. Nonetheless, this particular ice-coupled experiment represents a useful illustration of side effects of the phase mixing approach proposed to constrain the numerical instability of our GKE algorithm. It is generally believed that fast evolution takes place (i) when the initial spectrum is far from its statistical equilibrium and (ii) when the assumed initial probability distribution of waves (typically

Gaussian with zero fourth-order cumulant and $I(t)$ does not match the underlying spectrum (Janssen 2003; Annenkov & Shrira 2006, GS13). Phase mixing causes periodic mismatch between the kurtosis and spectrum (figure 13 of Annenkov & Shrira 2016), and therefore may provoke stronger but likely spurious spectral evolution. GS13 (their figure 13) has demonstrated this effect nicely for the 1-D spectrum.

7. Limitations of the GKE algorithm

7.1. Phase mixing and high-frequency instability

In nearly all the GKE/JKE simulations, the wave spectrum, after a sufficiently long time, developed high-frequency instability and eventually the simulations became numerically unstable (figure 14; see also figure 6 of AS18). Currently, the nature of such high-frequency instabilities is not fully understood. It may be physical, being partly related to wave breaking (GB16, see also Longuet-Higgins & Cokelet 1976). It is also worth mentioning that high-frequency instability is commonly seen in the computations of nonlinear surface waves and capillary waves (Longuet-Higgins & Cokelet 1976; Dommermuth & Yue 1987; Pushkarev & Zakharov 2000).

In the context of numerical realizations of the GKE, phase mixing (randomization), first proposed by GS13, is the only effective way of suppressing these high-frequency instabilities discussed in the literature (figure 14). It is observed that after the cold start (the initial state with totally random, uncorrelated phases), the instabilities take some time to develop. By randomizing the phases periodically the instabilities are prevented from disrupting the computations. It should be emphasized that the phase mixing approach is an approximation, and at the moment the accuracy of this approximation is not very clear. In the extreme, ice-coupled case, model results do show sensitivity to the adopted frequency of phase mixing (figure 11). Other techniques such as low-pass filtration (frequency-dependent damping term; Dommermuth & Yue 1987; Pushkarev & Zakharov 2000; Tolman 2011) may be experimented with the GKE in the future.

It should also be mentioned that the randomization, on the other hand, may facilitate fast evolution (figure 11) for the reasons explained in the previous section. For other cases explored in this paper, the GKE and JKE do not deviate significantly from the HKE even though phase mixing is activated. Therefore, these results are believed to be robust. Further discussion about phase mixing can be found in Annenkov & Shrira (2016).

7.2. Applicability for 2-D simulations

All the simulations presented in this paper were performed with a single grid point version of WW3. Despite this very simple scenario, the long-term GKE runs ($O(10^3)$ wave periods) are computationally challenging. First, for the spectral grids we used, simulations with the GKE require interactions of enormous quasi-resonant and resonant quadruplets ($O(10^7 \sim 10^8)$) to be calculated. Second, as already pointed out, it is difficult to obtain the analytic form of the diagonal term for the GKE nonlinear transfer, and therefore we have used the explicit yet more time-consuming scheme to integrate source terms. Owing to these factors, the GKE runs are approximately 5–10 times more expensive than the HKE (see also figure 3 of GB16). It should be noted, however, that the same as the WRT, our GKE algorithm is not parallelized, and thus all the simulations presented here were run on a single processor. A more efficient, parallel GKE algorithm has been developed by Annenkov & Shrira (2016), and their GKE could outrun the HKE when using sufficient processors.

Applying the GKE onto a 2-D spatial domain could be more demanding. The periodic phase mixing is unavoidably desired to suppress the high-frequency noise. However, in this way, we could easily end up with a situation where wave phases at two neighbouring grid points are mixed at different instants due to their distinct wave periods. This might cause numerical problems as well, especially when one spectrum with some slightly perturbed high-frequency modes is spatially advected to the downstream grid points. Apart from this difficulty, we need a 2-D $N_q \times N_{sea}$ matrix to trace the previous history of wave evolution over the whole 2-D model domain, where N_q is the total number of unique quadruplets (appendix A) and N_{sea} is the total number of sea grid points. Obviously, storing this matrix in the internal memory will soon become impossible as N_{sea} increases. All these limitations of our GKE algorithm would practically inhibit its large-scale, realistic applications. Andrade, Stuhlmeier & Stiassnie (2019) reported that when applied to degenerate quartets, the GKE may exhibit blow-up under certain conditions, further implying a possible inherent deficiency of the GKE. Such strange behaviour, however, is not observed in our simulations for wave spectra with multiple wave modes.

8. Concluding remarks

The HKE (Hasselmann 1962), formulating the nonlinear transfer due to resonant four-wave interactions, stands for the most fundamental component of contemporary spectral wave models. The useful parameterization of this critical nonlinear process developed in 1980s, i.e. the discrete interaction approximation (Hasselmann *et al.* 1985), directly opened up a new generation of spectral wave modelling, and is still routinely employed in present-day operational wave forecast and hindcast. More accurate yet economic alternative parameterizations have been proposed over the last three decades (e.g. Komatsu & Masuda 1996; Polnikov 1997; Benoit 2005; Resio & Perrie 2008; Tolman 2013). Meanwhile, effort has also been put into establishing alternative kinetic equations that take into account non-resonant four-wave interactions and therefore are expected to outperform the HKE in describing fast evolution of wave fields and possibly in predicting the occurrence of freak waves due to modulational instability (Janssen 2003; Annenkov & Shrira 2006; Onorato *et al.* 2009; Waseda, Kinoshita & Tamura 2009; Xiao *et al.* 2013, GS13, among others). For 1-D spectra, the advantage of modern kinetic equations (JKE, GKE) over the HKE is beyond controversy (Janssen 2003, GS13). For directional wave spectra, however, findings from previous studies, particularly GB16 and Annenkov & Shrira (2015, 2016, 2018), are not fully consistent.

Dedicated to resolving these disputes, this study has scrutinized the GKE algorithm of GB16 and identified two numerical defects related to the discretization of the GKE and to source term integration. It is proved that once these numerical flaws are amended, our results now are comparable to those reported by Annenkov & Shrira. Key findings are summarized as follows.

- (i) For the open-water, duration-limited wave growth case, all the three equations (HKE, JKE and GKE) yield very similar growth curves (figure 3), provided that the phase mixing approach is applied to stabilize the JKE/GKE simulations. Under this steady wind forcing, traditional wave parameters H_s and f_p are practically insensitive to the frequency of phase mixing (N_{pm}), as already demonstrated in GS13 and Annenkov & Shrira (2016).
- (ii) In line with Annenkov & Shrira (2015), even for wave spectra subject to turning winds (i.e. a sudden change in wind direction), the GKE/JKE produces comparable results to the HKE. Surprisingly, the average directional response time scale, as

yielded by the state-of-the-art source term package (ST6), does not significantly deviate from that given by the source term package developed some 30 years ago (figure 9). For old waves, the simulated rate of spectral turning is considerably lower than observations (VH93), possibly highlighting deficiencies in model source terms in these situations.

- (iii) For the experiment with the steep Gaussian spectrum, the relaxation of the rear face of wave spectrum to the f^{-4} high-frequency decay noticeably differs across different kinetic equation simulations. The growth rate of the tail is seen as $\text{GKE} >_{\epsilon} \text{JKE} > \text{HKE}$ (figure 5; here ‘ $>_{\epsilon}$ ’ means ‘marginally greater than’). We analysed the scaling of the maximum growth rate S_{nl}^{max} with wave steepness ϵ , and found that the HKE corresponds to $S_{nl}^{max} \sim \epsilon^6$ and the JKE/GKE to $S_{nl}^{max} \sim \epsilon^{5.5}$ (figure 8), again in good agreement with AS18. The most striking result in this paper, in our opinion, is that the HKE and JKE/GKE initially operate at the same fast $O(1/\epsilon^2\omega_0)$ time scale for the spectral peak downshift and angular spreading (figure 6). This is apparently contrary to the generally accepted viewpoint that the HKE only prescribes spectral evolution on a slow $O(1/\epsilon^4\omega_0)$ time scale (Hasselmann 1962; Dysthe *et al.* 2003; Janssen 2003). Despite being counter-intuitive, we stress that this finding was already evident in simulations conducted by AS18 (their figure 8).
- (iv) The ice-coupled experiment represents the only case where we found that the GKE/JKE indeed produces remarkably faster wave growth than the HKE (figure 11) yet as a result of multiple uncommon factors. The GKE runs are shown to be sensitive to the frequency of phase mixing, further obfuscating the problem being investigated.
- (v) The JKE and GKE provide almost identical results even for the ice-coupled test where wave spectrum is not smooth during the early stage of development (figures 11 and 12). This implies the assumption that the action density is slowly varying (i.e. independent on the fast time scale), as adopted by the JKE (Janssen 2004, § 4.5), may be reasonably valid.

To sum up, we believe our paper has clarified the open question regarding differences in spectral evolution of directional wave fields according to different kinetic equations. Given the results presented here and previously reported by Annenkov & Shrira, it appears sensible to conclude that dissimilar to the 1-D spectrum case, the GKE and JKE, unexpectedly, do not produce significantly different development of 2-D spectra, provided that wave spectra are fairly smooth and the directionality is sufficiently broad. In other words, it appears that the HKE, solved by the well-established WRT algorithm, works more robustly than what is usually expected from its formulation, particularly in terms of the fast evolution of f_p and σ_{θ} on a ‘dynamic’ $O(1/\epsilon^2\omega_0)$ time scale. It might be likely that the WRT algorithm, when discretizing the HKE, ‘fails’ to stay exactly at the resonance loci and therefore introduces some quasi-resonant effect. Alternatively, the time scaling ($O(1/\epsilon^2\omega_0)$ or $O(1/\epsilon^4\omega_0)$) may only apply to discrete wave components $N(k, \theta, t)$ but not necessarily apply to any integral wave parameters (e.g. f_p and σ_{θ} ; S. Annenkov, personal communication, 2020). One of our reviewers also suggested that the spectral peak downshift and angular spreading are manifestations of the self-similar evolution of the wave field (Badulin *et al.* 2005, 2007), and are not directly linked to the dN/dt scaling.

The scope of the present paper is limited to investigating different kinetic equations in a spectral wave model. Nonetheless, it is noteworthy that Annenkov & Shrira (2018, 2019) inter-compared the HKE, GKE and direct simulations based on the Zakharov equation (DNS-ZE), and found that the two kinetic equations, being close to each other, behave markedly differently from the DNS-ZE in shaping the spectrum. Wave spectra

from the DNS-ZE are angularly less spread but broader in the frequency space with less-pronounced spectral peaks. Liu *et al.* (2019) demonstrated that the HKE, together with the ST6 package, overestimates spectral peakedness of the fetch-limited wind waves, providing an indirect support of these findings. It may be feasible to further explore these discrepancies and the directional response of ocean waves to turning winds by employing the three-dimensional, fully nonlinear phase-resolving wave model established by Chalikov (2018) in which effects of wind input and wave breaking are reasonably parameterized.

Acknowledgements. The authors are grateful to Dr P. Janssen (ECMWF), Dr S. Annenkov (Keele University) and Dr D. Barratt (University of Oxford) for very helpful discussion about kinetic equations. We appreciate Dr A. Pushkarev and anonymous reviewers for very constructive comments that significantly improved this paper.

Funding. Q.L. acknowledges the support from the DISI Australia–China Centre through Grant ACSRF48199. A.V.B. appreciates the financial support from the US Office of Naval Research Grant N00014-17-1-3021-A00001.

Declaration of interests. The authors report no conflict of interest.

Author ORCIDs.

- Qingxiang Liu <http://orcid.org/0000-0001-6100-0221>;
- Odin Gramstad <http://orcid.org/0000-0001-7531-3595>;
- Alexander Babanin <http://orcid.org/0000-0002-8595-8204>.

Appendix A. Numerical implementation of the GKE

When implemented in WW3, (2.3)–(2.7) for the GKE are solved by the following steps.

- (i) For a given 2-D (f, θ) grid consisting of N_f frequencies and N_θ directions, we first transform it into a wavenumber grid (k_x, k_y), of which each component (k_x or k_y) is stored in a 1-D array with $N_s = N_f N_\theta$ elements. The corresponding area of each wavenumber bin $\delta k = k \delta k \delta \theta = k \delta \omega \delta \theta / c_g$ is recorded in another 1-D array.
- (ii) Based on the known (k_x, k_y) grid, we find all the *unique* interactive quadruplets satisfying (2.9) and the following criteria:

$$\left. \begin{aligned} i_2 &\geq i_1, \\ i_3 &\neq i_1, \quad i_3 \neq i_2, \\ i_4 &\geq i_3, \\ i_4 &\neq i_1, \quad i_4 \neq i_2, \\ i_1 + (i_2 - 1) \times N_s &< i_3 + (i_4 - 1) \times N_s, \end{aligned} \right\} \quad (A1)$$

where i_j refers to the index of k_j in the 1-D k_x and k_y arrays: k_1, k_2 and k_3 are chosen at the wavenumber grid points; k_4 is naturally determined by (2.9); and i_4 is approximated by the index of the wavenumber grid point nearest to k_4 .

The criteria (A1) are established to guarantee the uniqueness of the located quartets because a quadruplet (k_1, k_2, k_3, k_4) is essentially same as the following seven other

quadruplets (Hasselmann & Hasselmann 1985):

$$\left. \begin{aligned} &(k_2, k_1, k_3, k_4), \\ &(k_1, k_2, k_4, k_3), \\ &(k_2, k_1, k_4, k_3), \\ &(k_3, k_4, k_1, k_2), \\ &(k_3, k_4, k_2, k_1), \\ &(k_4, k_3, k_1, k_2), \\ &(k_4, k_3, k_2, k_1). \end{aligned} \right\} \quad (\text{A2})$$

Meanwhile, the last criterion of (A1) already indicates that any quantity for the quadruplets (e.g. $\Delta\omega$, $T_{1,2,3,4}$, $\mathcal{F}_{1,2,3,4}$) can be stored in a sparse upper triangular $N_s^2 \times N_s^2$ matrix. A given quadruplet (k_1, k_2, k_3, k_4) corresponds to the entry in the r th row and c th column of that sparse matrix, where

$$\left. \begin{aligned} r &= i_1 + (i_2 - 1) \times N_s, \\ c &= i_3 + (i_4 - 1) \times N_s, \end{aligned} \right\} \quad (\text{A3})$$

as clearly illustrated in figure 13.

- (iii) Calculate the nonlinear transfer rates $\mathcal{M}_{1,2,3,4}$ (2.4)–(2.7) for all the unique quartets and record these values in a sparse upper triangular matrix $\mathbf{M}_{1,2,3,4}$ ($N_s^2 \times N_s^2$; figure 13, leftmost)
- (iv) According to the property of detailed balance $\delta C_1 = -\delta C_3 = -\delta C_4$ (see (2.2)), we can integrate interaction contributions over all (k_3, k_4) by

$$\mathbf{M}_{1,2} = (\mathbf{M}_{1,2,3,4} - \mathbf{M}_{1,2,3,4}^T) \times \mathbf{S}_{3,4}, \quad (\text{A4})$$

where $\mathbf{S}_{3,4}$ is a $N_s^2 \times 1$ column vector (figure 13, middle):

$$\mathbf{S}_{3,4} = \begin{cases} 1, & k_3 = k_4, \\ 2, & k_3 \neq k_4. \end{cases} \quad (\text{A5})$$

- (v) Reshape $\mathbf{M}_{1,2}$ in (A4) as a $N_s \times N_s$ upper triangular matrix (figure 13, rightmost) and integrate contributions over all k_2 ($\delta C_1 = \delta C_2$):

$$\left(\frac{dC_1}{dt} \delta k_1 \right)_{N_s \times 1} = \sum_{k_2} (\mathbf{M}_{1,2} + \mathbf{M}_{1,2}^T) \odot \mathbf{S}_{1,2}, \quad (\text{A6})$$

where \odot denotes element-wise multiplication, $\mathbf{S}_{1,2}$ is a 2-D $N_s \times N_s$ matrix

$$\mathbf{S}_{1,2} = \begin{cases} 1/2, & k_1 = k_2, \\ 1, & k_1 \neq k_2. \end{cases} \quad (\text{A7})$$

Thus far, the calculation of the GKE-predicted growth rate dC_1/dt (2.3) is completed, and the nonlinear transfer $S_{nl}(k, \theta)$ required by WW3 is obtained through (1.6).

It is noteworthy that when the phase mixing approach is not employed (§ 2.1), the GKE/JKE-simulated wave spectra will become noisy after long times of model integration and eventually lead to unrealistic wave growth behaviour (figure 14). Re-mixing of wave phases by every $O(10^2)$ wave periods will effectively suppress these high-frequency noises and produce smooth, reasonable evolution of wind wave spectra.

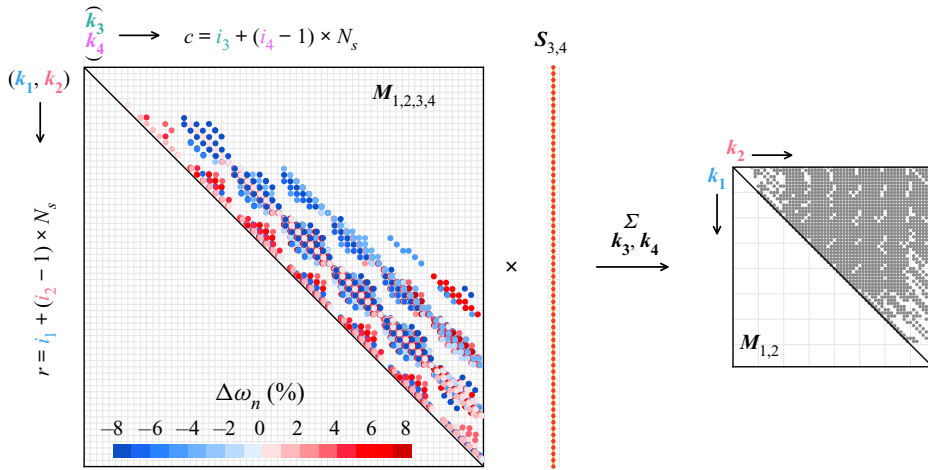


Figure 13. Illustration of the GKE algorithm on a very coarse (f, θ) grid: $f_i = 0.04 \times 1.1^{i-1}$, $i = 1, \dots, 8$, and $\theta \in [-120^\circ, 120^\circ]$ with $\Delta\theta = 30^\circ$. The colour of elements of $M_{1,2,3,4}$ indicates the normalized frequency mismatch for a given quartet $\Delta\omega_n = \Delta\omega / \min(\omega_1, \omega_2, \omega_3, \omega_4)$.

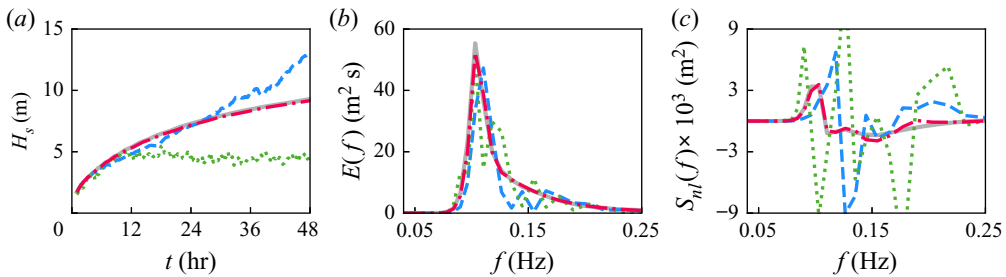


Figure 14. (a) Evolution of the significant wave height H_s in the duration-limited test under $U_{10} = 20 \text{ m s}^{-1}$ (§ 3). (b) Wave spectrum $E(f)$ and (c) nonlinear transfer $S_{nl}(f)$ after 11 h of model integration. Grey solid line, HKE; blue dashed line, GKE without phase mixing ($N_{pm} = \infty$); green dotted line, JKE without phase mixing; red dash-dotted line, GKE with phase mixing by every 100 wave periods. The phase-mixed JKE results basically overlap with the red line and thus are not shown.

Appendix B. Integral wave parameters from the wave spectrum

The bulk parameters selected in this study, including significant wave height H_s , mean wave period $T_{0,-1}$, $T_{0,2}$, Goda’s spectral narrowness Q_p , mean square slope $\langle s^2 \rangle$, mean wave direction θ_w , angular spreading σ_θ , are calculated from the 1-D and 2-D wave spectra $(E(f), F(f, \theta))$ as follows (Goda 2010, WW3DG2019):

$$m_n = \int f^n E(f) df, \tag{B1}$$

$$H_s = 4\sqrt{m_0}, \tag{B2}$$

$$T_{0,-1} = m_{-1}/m_0, \tag{B3}$$

$$T_{0,2} = \sqrt{m_0/m_2}, \tag{B4}$$

$$Q_p = \frac{2}{m_0^2} \int f E^2(f) df, \quad (\text{B5})$$

$$\langle s^2 \rangle = \int k^2 E(f) df, \quad (\text{B6})$$

$$a = \iint \cos \theta F(f, \theta) df d\theta, \quad (\text{B7})$$

$$b = \iint \sin \theta F(f, \theta) df d\theta, \quad (\text{B8})$$

$$\theta_w = \arctan(b/a), \quad (\text{B9})$$

$$\sigma_\theta = \sqrt{2 \left(1 - \sqrt{(a^2 + b^2)/m_0^2} \right)}. \quad (\text{B10})$$

The peak frequency f_p is estimated from $E(f)$ using a parabolic fit in the neighbourhood of the discrete spectral peak. When necessary, we also fit the generalized JONSWAP spectral form (Young 2006)

$$E(f) = \alpha g^2 (2\pi)^{-4} f_p^{-(5+n)} f^n \exp \left[\frac{n}{4} \left(\frac{f}{f_p} \right)^{-4} \right] \times \gamma \exp \left[-(f-f_p)^2 / 2\sigma^2 f_p^2 \right], \quad (\text{B11})$$

to the simulated wave spectra and record the corresponding high-frequency energy level α and peak enhancement factor γ . For $n = -5$, (B11) corresponds to the JONSWAP form of Hasselmann *et al.* (1973) and for $n = -4$ to the form proposed by Donelan, Hamilton & Hui (1985). The fitting approach can be found in Liu *et al.* (2019, their § 4.c).

REFERENCES

- ANDRADE, D., STUHLMEIER, R. & STIASSNIE, M. 2019 On the generalized kinetic equation for surface gravity waves, blow-up and its restraint. *Fluids* **4** (1), 2.
- ANNENKOV, S. Y. & SHRIRA, V. I. 2006 Role of non-resonant interactions in the evolution of nonlinear random water wave fields. *J. Fluid Mech.* **561**, 181–207.
- ANNENKOV, S. Y. & SHRIRA, V. I. 2009 “Fast” nonlinear evolution in wave turbulence. *Phys. Rev. Lett.* **102** (2), 1–4.
- ANNENKOV, S. Y. & SHRIRA, V. I. 2015 Modelling the impact of squall on wind waves with the generalized kinetic equation. *J. Phys. Oceanogr.* **45** (3), 807–812.
- ANNENKOV, S. Y. & SHRIRA, V. I. 2016 Modelling transient sea states with the generalised kinetic equation. In *Rogue and Shock Waves in Nonlinear Dispersive Media* (ed. M. Onorato, S. Residori & F. Baronio), pp. 159–178. Springer.
- ANNENKOV, S. Y. & SHRIRA, V. I. 2018 Spectral evolution of weakly nonlinear random waves: kinetic description versus direct numerical simulations. *J. Fluid Mech.* **844**, 766–795.
- ANNENKOV, S. Y. & SHRIRA, V. I. 2019 Modelling evolution of directional spectra of water waves. In *Workshop on Nonlinear Water Waves, RIMS Kokyuroku* (ed. S. Murashige), vol. 2109, pp. 100–114. Kyoto University.
- BABANIN, A. V., CHALIKOV, D., YOUNG, I. R. & SAVELYEV, I. 2010 Numerical and laboratory investigation of breaking of steep two-dimensional waves in deep water. *J. Fluid Mech.* **644**, 433–463.
- BABANIN, A. V., YOUNG, I. R. & BANNER, M. L. 2001 Breaking probabilities for dominant surface waves on water of finite constant depth. *J. Geophys. Res.* **106**, 11659.
- BADULIN, S. I., BABANIN, A. V., ZAKHAROV, V. E. & RESIO, D. 2007 Weakly turbulent laws of wind-wave growth. *J. Fluid Mech.* **591**, 339–378.
- BADULIN, S. I., PUSHKAREV, A. N., RESIO, D. & ZAKHAROV, V. E. 2005 Self-similarity of wind-driven seas. *Nonlinear. Process. Geophys.* **12** (6), 891–945.
- BARSTOW, S. F., *et al.* 2005 *Measuring and Analysing the Directional Spectrum of Ocean Waves*. COST Office.

Kinetic equations in a third-generation spectral wave model

- BENOIT, M. 2005 Evaluation of methods to compute the non-linear quadruplet interactions for deep-water wave spectra. In *Proceedings of the Fifth International Symposium on Ocean Waves Measurement and Analysis* (ed. B.L. Edge & J.C. Santas), pp. 1–10. IAHR Secretariat.
- BIDLOT, J.-R. 2001 ECMWF wave-model products. *ECMWF Newsl.* **91**, 9–15.
- CAVALERI, L., *et al.* 2007 Wave modelling – the state of the art. *Prog. Oceanogr.* **75** (4), 603–674.
- CAVALERI, L., *et al.* 2018 Wave modelling in coastal and inner seas. *Prog. Oceanogr.* **167**, 164–233.
- CHALIKOV, D. 2018 Numerical modeling of surface wave development under the action of wind. *Ocean Sci.* **14** (3), 453–470.
- CHENG, S., *et al.* 2017 Calibrating a viscoelastic sea ice model for wave propagation in the arctic fall marginal ice zone. *J. Geophys. Res.* **122** (11), 8770–8793.
- DOMMERMUTH, D.G. & YUE, D.K.P. 1987 A high-order spectral method for the study of nonlinear gravity waves. *J. Fluid Mech.* **184**, 267–288.
- DONELAN, M.A., BABANIN, A.V., YOUNG, I.R. & BANNER, M.L. 2006 Wave-follower field measurements of the wind-input spectral function. Part II: parameterization of the wind input. *J. Phys. Oceanogr.* **36** (8), 1672–1689.
- DONELAN, M.A., HAMILTON, J. & HUI, W.H. 1985 Directional spectra of wind-generated waves. *Phil. Trans. R. Soc. Lond. A* **315** (1534), 509–562.
- DYSTHE, K.B., TRULSEN, K., KROGSTAD, H.E. & SOCQUET-JUGLARD, H. 2003 Evolution of a narrow-band spectrum of random surface gravity waves. *J. Fluid Mech.* **478**, 1–10.
- GODA, Y. 2010 *Random Seas and Design of Maritime Structures*. World Scientific.
- GRAMSTAD, O. & BABANIN, A. 2016 The generalized kinetic equation as a model for the nonlinear transfer in third-generation wave models. *Ocean Dyn.* **66** (4), 509–526.
- GRAMSTAD, O. & STIASSNIE, M. 2013 Phase-averaged equation for water waves. *J. Fluid Mech.* **718**, 280–303.
- HASSELMANN, K. 1962 On the non-linear energy transfer in a gravity-wave spectrum. Part I. General theory. *J. Fluid Mech.* **12** (4), 481–500.
- HASSELMANN, K., *et al.* 1973 Measurements of wind-wave growth and swell decay during the Joint North Sea Wave Project (JONSWAP). *Tech. Rep.* Deutsches Hydrographisches Institut.
- HASSELMANN, S. & HASSELMANN, K. 1985 Computations and parameterizations of the nonlinear energy transfer in a gravity-wave spectrum. Part I: a new method for efficient computations of the exact nonlinear transfer integral. *J. Phys. Oceanogr.* **15** (11), 1369–1377.
- HASSELMANN, S., HASSELMANN, K., ALLENDER, J.H. & BARNETT, T.P. 1985 Computations and parameterizations of the nonlinear energy transfer in a gravity-wave spectrum. Part II: parameterizations of the nonlinear energy transfer for application in wave models. *J. Phys. Oceanogr.* **15** (11), 1378–1392.
- HOLTHUIJSEN, L.H. 2007 *Waves in Oceanic and Coastal Waters*. Cambridge University Press.
- JANSSEN, P.A.E.M. 2003 Nonlinear four-wave interactions and freak waves. *J. Phys. Oceanogr.* **33** (4), 863–884.
- JANSSEN, P.A.E.M. 2004 *The Interaction of Ocean Waves and Wind*. Cambridge University Press.
- JANSSEN, P.A.E.M. 2008 Progress in ocean wave forecasting. *J. Comput. Phys.* **227** (7), 3572–3594.
- JANSSEN, P.A.E.M. 2009 On some consequences of the canonical transformation in the Hamiltonian theory of water waves. *J. Fluid Mech.* **637**, 1–44.
- JANSSEN, P.A.E.M. & JANSSEN, A.J.E.M. 2019 Asymptotics for the long-time evolution of kurtosis of narrow-band ocean waves. *J. Fluid Mech.* **859**, 790–818.
- JANSSEN, P.A.E.M., LIONELLO, P., REISTAD, M. & HOLLINGSWORTH, A. 1989 Hindcasts and data assimilation studies with the WAM model during the Seasat period. *J. Geophys. Res.* **94** (C1), 973–993.
- KOMATSU, K. & MASUDA, A. 1996 A new scheme of nonlinear energy transfer among wind waves: RIAM method-algorithm and performance. *J. Oceanogr.* **52** (4), 509–537.
- KOMEN, G.J., CAVALERI, L., DONELAN, M.A., HASSELMANN, K., HASSELMANN, S. & JANSSEN, P.A.E.M. 1994 *Dynamics and Modelling of Ocean Waves*. Cambridge University Press.
- KOMEN, G.J., HASSELMANN, K. & HASSELMANN, K. 1984 On the existence of a fully developed wind-sea spectrum. *J. Phys. Oceanogr.* **14** (8), 1271–1285.
- KRASITSKII, V.P. 1994 On reduced equations in the Hamiltonian theory of weakly nonlinear surface waves. *J. Fluid Mech.* **272** (5), 1–20.
- LIU, Q., ROGERS, W.E., BABANIN, A., LI, J. & GUAN, C. 2020 Spectral modeling of ice-induced wave decay. *J. Phys. Oceanogr.* **50** (6), 1583–1604.
- LIU, Q., ROGERS, W.E., BABANIN, A.V., YOUNG, I.R., ROMERO, L., ZIEGER, S., QIAO, F. & GUAN, C. 2019 Observation-based source terms in the third-generation wave model WAVEWATCH III: updates and verification. *J. Phys. Oceanogr.* **49** (2), 489–517.

- LONGUET-HIGGINS, M.S. & COKELET, E.D. 1976 The deformation of steep surface waves on water. I. A numerical method of computation. *Proc. R. Soc. Lond. A* **350** (1660), 1–26.
- MASSON, D. & LEBLOND, P.H. 1989 Spectral evolution of wind-generated surface gravity waves in a dispersed ice field. *J. Fluid Mech.* **202** (-1), 43.
- MEYLAN, M.H., BENNETTS, L.G., MOSIG, J.E.M., ROGERS, W.E., DOBLE, M.J. & PETER, M.A. 2018 Dispersion relations, power laws, and energy loss for waves in the marginal ice zone. *J. Geophys. Res.* **123**, 1–13.
- ONORATO, M., *et al.* 2009 Statistical properties of mechanically generated surface gravity waves: a laboratory experiment in a three-dimensional wave basin. *J. Fluid Mech.* **627**, 235–257.
- ONORATO, M., OSBORNE, A.R., SERIO, M., CAVALERI, L., BRANDINI, C. & STANSBERG, C.T. 2006 Extreme waves, modulational instability and second order theory: wave flume experiments on irregular waves. *Eur. J. Mech. B/Fluids* **25** (5), 586–601.
- ONORATO, M., OSBORNE, A.R., SERIO, M., RESIO, D., PUSHKAREV, A., ZAKHAROV, V.E. & BRANDINI, C. 2002 Freely decaying weak turbulence for sea surface gravity waves. *Phys. Rev. Lett.* **89** (14), 144501.
- POLNIKOV, V.G. 1997 Nonlinear energy transfer through the spectrum of gravity waves for the finite depth case. *J. Phys. Oceanogr.* **27** (8), 1481–1491.
- POLNIKOV, V.G. & LAVRENOV, I.V. 2007 Calculation of the nonlinear energy transfer through the wave spectrum at the sea surface covered with broken ice. *Oceanology* **47** (3), 334–343.
- PUSHKAREV, A.N. & ZAKHAROV, V.E. 2000 Turbulence of capillary waves—theory and numerical simulation. *Physica D* **135** (1–2), 98–116.
- RESIO, D.T. & PERRIE, W. 1991 A numerical study of nonlinear energy fluxes due to wave-wave interactions. Part I: methodology and basic results. *J. Fluid Mech.* **223**, 603–629.
- RESIO, D.T. & PERRIE, W. 2008 A two-scale approximation for efficient representation of nonlinear energy transfers in a wind wave spectrum. Part I: theoretical development. *J. Phys. Oceanogr.* **38** (12), 2801–2816.
- ROGERS, W.E., BABANIN, A.V. & WANG, D.W. 2012 Observation-consistent input and whitecapping dissipation in a model for wind-generated surface waves: description and simple calculations. *J. Atmos. Ocean. Technol.* **29** (9), 1329–1346.
- ROGERS, W.E., MEYLAN, M. & KOHOUT, A.L. 2018 Frequency distribution of dissipation of energy of ocean waves by sea ice using data from Wave Array 3 of the ONR “Sea State” field experiment. *Tech. Rep.* Naval Research Laboratory, Stennis Space Center, MS 39529–5004. Available at <https://www7320.nrlssc.navy.mil/pubs/2018/rogers2-2018.pdf>.
- ROGERS, W.E., THOMSON, J., SHEN, H.H., DOBLE, M.J., WADHAMS, P. & CHENG, S. 2016 Dissipation of wind waves by pancake and frazil ice in the autumn Beaufort Sea. *J. Geophys. Res.* **121** (11), 7991–8007.
- ROMERO, L. & MELVILLE, W.K. 2010 Airborne observations of fetch-limited waves in the Gulf of Tehuantepec. *J. Phys. Oceanogr.* **40** (3), 441–465.
- SHRIRA, V.I. & ANNENKOV, S.Y. 2013 Towards a new picture of wave turbulence. In *Advances in Wave Turbulence* (ed. V. Shrira & S. Nazarenko), pp. 239–281. World Scientific.
- THE WAMDI GROUP 1988 The WAM model – a third generation ocean wave prediction model. *J. Phys. Oceanogr.* **18** (12), 1775–1810.
- THE WAVEWATCH III® DEVELOPMENT GROUP (WW3DG) 2019 User manual and system documentation of WAVEWATCH III® version 6.07. *Tech. Note* 333. NOAA/NWS/NCEP/MMAB, College Park, MD, USA, 465 pp. + Appendices.
- TOLMAN, H.L. 1992 Effects of numerics on the physics in a third-generation wind-wave model. *J. Phys. Oceanogr.* **22** (10), 1095–1111.
- TOLMAN, H.L. 2009 User manual and system documentation of wavewatch III version 3.14. *Tech. Rep.* 276. NOAA/NWS/NCEP/MMAB, 194 pp. + Appendices.
- TOLMAN, H.L. 2011 A conservative nonlinear filter for the high-frequency range of wind wave spectra. *Ocean Model.* **39** (3–4), 291–300.
- TOLMAN, H.L. 2013 A generalized multiple discrete interaction approximation for resonant four-wave interactions in wind wave models. *Ocean Model.* **70**, 11–24.
- TRACY, B. & RESIO, D.T. 1982 Theory and calculation of the nonlinear energy transfer between sea waves in deep water. *WES Report* 11. US Army Corps of Engineers.
- VAN VLEDDER, G.P. 2000 Improved method for obtaining the integration space for the computation of nonlinear quadruplet wave-wave interaction. In *Proceedings of the 6th International Workshop on Wave Forecasting and Hindcasting* (ed. D.T. Resio), pp. 418–431. Meteorological Service of Canada, Environment Canada.
- VAN VLEDDER, G.P. 2006 The WRT method for the computation of non-linear four-wave interactions in discrete spectral wave models. *Coast. Engng* **53** (2–3), 223–242.

Kinetic equations in a third-generation spectral wave model

- VAN VLEDDER, G.P. & HOLTHUIJSEN, L.H. 1993 The directional response of ocean waves to turning winds. *J. Phys. Oceanogr.* **23** (2), 177–192.
- WADHAMS, P., SQUIRE, V.A., EWING, J.A. & PASCAL, R.W. 1986 The effect of the marginal ice zone on the directional wave spectrum of the ocean. *J. Phys. Oceanogr.* **16** (2), 358–376.
- WASEDA, T., KINOSHITA, T. & TAMURA, H. 2009 Evolution of a random directional wave and freak wave occurrence. *J. Phys. Oceanogr.* **39** (3), 621–639.
- WEBB, D.J. 1978 Non-linear transfers between sea waves. *Deep-Sea Res.* **25** (3), 279–298.
- XIAO, W., LIU, Y., WU, G. & YUE, D.K.P. 2013 Rogue wave occurrence and dynamics by direct simulations of nonlinear wave-field evolution. *J. Fluid Mech.* **720**, 357–392.
- YOUNG, I.R. 1999 *Wind Generated Ocean Waves*. Elsevier Science Ltd.
- YOUNG, I.R. 2006 Directional spectra of hurricane wind waves. *J. Geophys. Res.* **111** (8), 1–14.
- YOUNG, I.R. & VAN VLEDDER, G.P. 1993 A review of the central role of nonlinear interactions in wind-wave evolution. *Phil. Trans. R. Soc. Lond. A* **342** (1666), 505–524.
- ZAKHAROV, V.E. 1968 Stability of periodic waves of finite amplitude on the surface of a deep fluid. *J. Appl. Mech. Tech. Phys.* **9** (2), 190–194.
- ZIEGER, S., BABANIN, A.V., ROGERS, W.E. & YOUNG, I.R. 2015 Observation-based source terms in the third-generation wave model WAVEWATCH. *Ocean Model.* **218**, 1–24.